JOURNAL OF PETROLOGY | VOLUME 42 | NUMBER 7 | PAGES 1301–1320 | 2001

High f_{O_2} During Sillimanite Zone Metamorphism of Part of the Barrovian Type Locality, Glen Clova, Scotland

JAY J. AGUE*, ETHAN F. BAXTER† AND JAMES O. ECKERT JR

DEPARTMENT OF GEOLOGY AND GEOPHYSICS, YALE UNIVERSITY, PO BOX 208109, NEW HAVEN, CT 06520-8109, USA

RECEIVED NOVEMBER 8, 1999; REVISED TYPESCRIPT ACCEPTED DECEMBER 5, 2000

The redox state of sillimanite zone (650–700°C, 5–6 kbar) metasediments of the Barrovian type area, Scotland, was investigated using estimates of metamorphic oxygen fugacity (f_{O_2}), sulfur fugacity (f_{S_2}), and fluid chemistry based on new determinations of mineral and rock compositions from 33 samples. A total of 94% of the samples lack graphite, contain both ilmenite–hematite solid solutions (RHOMOX) and magnetite, and had metamorphic f_{O_2} about 2 log_{10} units above the quartz–fayalite–magnetite (QFM) buffer. The regional variation in metamorphic f_{O_2} for these rocks was minimal, about $\pm 0{\cdot}3$ log_{10} units, reflecting either a protolith that was homogeneous with respect to redox state, or an initially variable protolith whose redox state was homogenized by metamorphic fluid–rock interaction. RHOMOX inclusions in garnet porphyroblasts that become richer in ilmenite from the interior to the edge of the host porphyroblast suggest that at least some syn-metamorphic reduction of rock occurred. Significant variations in bulk-rock oxidation ratio (OR) that are probably inherited from sedimentary protoliths are found from one layer to the next; OR ranges mostly between ~20 and ~50 [OR = molecular $2Fe_2O_3 \times 100/(2Fe_2O_3 + FeO)$]. These OR variations are uncorrelated with f_{O_2} and do not indicate that large, order-of-magnitude gradients in f_{O_2} and redox state existed or were preserved between layers during metamorphism. The other 6% of the samples contain ilmenite, lack magnetite, and had low f_{O_2} 0–1 order of magnitude below QFM in the stability field of graphite. They are characterized by combinations of the following: large fluid HF/H_2O; metasomatic, tourmaline-bearing veins; absence or rarity of primary organic matter; and crosscutting late metamorphic shear zones rich in carbonaceous material. Such observations suggest that locally low f_{O_2} conditions may have been related to the influx of reducing fluids from elsewhere in the area.

KEY WORDS: *metamorphism; redox; Barrovian; Scotland; oxygen fugacity*

INTRODUCTION

The chemical and mineralogical evolution of the crust during orogenesis is critically dependent upon the redox state of metamorphic fluids (James, 1955; Chinner, 1960; Buddington & Lindsley, 1964; Miyashiro, 1964; French, 1966; Eugster & Skippen, 1967; Thompson, 1970; Harte, 1975; Ohmoto & Kerrick, 1977; Rumble, 1978; Lamb & Valley, 1985; Frost, 1991*a*, 1991*b*; Brenan *et al.*, 1995; Harlov *et al.*, 1997; Ague, 1998). The classical Barrovian type locality in Glen Clova, Angus, Scotland, is a superb example of redox controls on metamorphism (Chinner, 1960). Based on field relations, petrography, and the chemical systematics of minerals and bulk rocks, Chinner (1960) showed that large differences in bulk-rock oxidation ratio (OR) existed at local and regional scales between metasediments during amphibolite facies metamorphism in Glen Clova [OR = molecular $2Fe_2O_3 \times 100/(2Fe_2O_3 + FeO)$]. These differences were attributed to chemical contrasts inherited, at least in part, from the sedimentary protoliths, and were taken as evidence that significant differences in f_{O_2} and fluid composition existed between layers during metamorphism (Chinner, 1960).

Rock oxidation ratio variations in Glen Clova have been unequivocally established, but important questions remain regarding the metamorphic fluids. For example, what were the quantitative variations in the fugacities of O_2 and sulfur species such as S_2 in the region? Did large variations in f_{O_2} and fluid composition exist between intercalated metasedimentary layers? Could metamorphic fluid–rock interaction between layers have overcome characteristic buffer capacities inherited from variable protoliths and act to homogenize redox states of fluids over the field area? In an effort to address these

*Corresponding author. Telephone: +1-203-432-3171. Fax: +1-203-432-3134. E-mail: jay.ague@yale.edu

†Present address: Division of Earth and Planetary Sciences, California Institute of Technology, MC 170-25, 1200 E. California Blvd., Pasadena, CA 91125, USA.

questions, we present a petrologic study of the Glen Clova rocks focused on quantification and interpretation of regional variations in the values of intensive variables during amphibolite facies Barrovian metamorphism. Our results suggest that regional mapping of metamorphic f_{O_2} and fluid compositions is useful for assessing possible redox state histories for the Barrovian type area. Throughout the text, we use the term 'redox state' in a general way to refer to the f_{O_2} and composition of metamorphic pore fluids.

GEOLOGIC RELATIONS

The metapelitic and metapsammitic rocks of Glen Clova form part of the Dalradian Supergroup and were deformed and metamorphosed during the Grampian orogeny (Harte *et al.*, 1984; Fettes *et al.*, 1986; Rogers *et al.*, 1989; Dempster & Bluck, 1995); peak metamorphism occurred at ~470 Ma (Oliver *et al.*, 2000; Baxter *et al.*, 2000). The timing of prograde porphyroblast growth relative to the four main deformational events (D_1–D_4) in the area can be summarized as follows (McLellan, 1989): (1) garnet: mostly syn-D_2, some syn- to post-D_3; (2) staurolite: syn- to post-D_2; (3) kyanite: pre- to syn-D_3; (4) sillimanite: mostly post-D_3. Some rocks also contain staurolite and kyanite that formed after sillimanite zone metamorphism and, presumably, after D_3 deformation (see Chinner, 1961; McLellan, 1985). The inferred bedding and the primary planar deformational fabric are subhorizontal (dips are $<\sim 30°$) and, thus, the rocks are part of the 'Flat Belt' of the Scottish Highlands (Harte *et al.*, 1984).

The Glen Clova area contains much loose float; we made every effort to sample only from fresh, *in situ* outcrops. We investigated rocks in and around Chinner's (1960) zone of 'Hematite-bearing gneisses and associated semipelitic gneisses' (Fig. 1), which our mapping indicates is at least 200–250 m thick. Chinner (1960) reported that at the margins of this zone the hematite-bearing rocks are intimately interbedded at the inch scale with hematite-free, graphite-bearing rocks, but we note that most of the graphitic rocks described in his paper are located 2–5·5 km away from the hematite-bearing zone. We were unable to confirm or refute the presence of such inch-scale interbedding during the course of our field and laboratory work.

McLellan (1985) inferred the main metamorphic reactions for the area. 'Peak' sillimanite zone conditions were ~650–700°C at ~6 kbar (McLellan, 1985), were probably accompanied by some degree of anatexis (McLellan, 1989), and may have required heat input by fluid advection (McLellan, 1989). No change in grade is evident across the field area, and most rocks retain some pre-sillimanite zone kyanite (Chinner, 1960, 1961; McLellan, 1985).

The oxide mineral assemblages provide a firm basis for subdivision of rock types. Chinner (1960) described assemblages of ilmenite + magnetite, ilmenite + magnetite + hematite, and hematite + magnetite. In addition, we recognize a fourth variety containing ilmenite alone.

PETROGRAPHIC RELATIONS

We present new compositional data for silicate and oxide minerals in 33 rocks from the Glen Clova area. Because Chinner (1960) provided data for garnet, muscovite, biotite, and rhombohedral oxide for his sample 11, we also consider this sample. Symbols are defined in Table 1, mineral assemblages are listed in Table 2, mineral compositions are given in Tables 3–6, and analytical and data reduction procedures are described in the Appendix.

Excellent petrographic descriptions of silicate assemblages have been given by many workers (e.g. Harry, 1958; Chinner, 1960, 1961; Harte & Johnson, 1969; McLellan, 1985, 1989). Consequently, we focus on the oxides and sulfides.

Prograde phases

The rhombohedral oxide (RHOMOX) minerals range primarily between ilmenite (Ilm) and hematite (Hem) in composition. RHOMOX are found throughout the rock matrix and as inclusions in garnet, aluminosilicate mineral, staurolite, and tourmaline porphyroblasts. Most crystals are subhedral to euhedral and 10–900 μm long. Unaltered RHOMOX in magnetite-bearing rocks contain exsolution lamellae; in many samples, these lamellae underwent additional fine-scale exsolution themselves (Fig. 2). The multiple sets of exsolution features almost certainly developed during progressive cooling from 'peak' T, as expected from phase relations in the Fe_2O_3–$FeTiO_3$ system (e.g. Burton, 1991), and suggest, although do not prove, that little chemical alteration of the grains occurred during cooling (Harlov *et al.*, 1997). Rocks without magnetite contain Ilm (X_{Ilm} >0·95) that lacks exsolution features.

Cubic solid solutions vary primarily between the magnetite (Mag) and ulvöspinel (Usp) endmembers, but are dominated by Mag ($X_{Mag} > \sim 0{\cdot}95$). Mag crystals are found in the rock matrix and, more rarely, as inclusions within porphyroblasts. Most grains are subhedral to euhedral and 10 and 1100 μm in diameter. Rare martite alteration of probable supergene origin is present in a few samples.

Rutile (Rt) is uncommon. Crystals are generally subhedral, ~100 μm long, and found in rock matrices

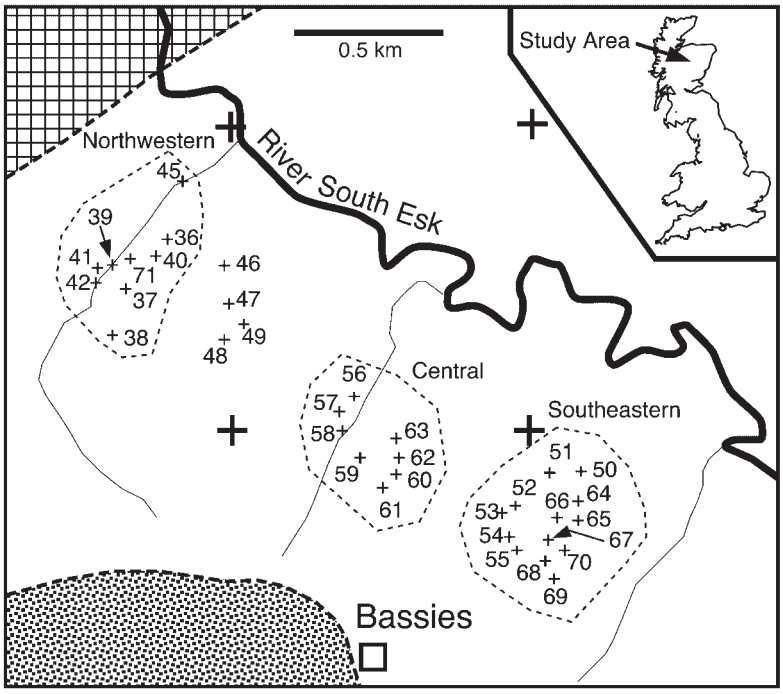

Fig. 1. Location map. Unpatterned area, amphibolite facies metasedimentary rocks; cross-hatch pattern, post-peak metamorphic intrusions ('Newer' igneous rocks); stipple, para-amphibolite ('Green Beds'). Samples used for northwestern, central, and southeastern profiles enclosed by dashed lines. Post-metamorphic, shallow-level, porphyritic dikes and sills omitted for clarity.

Table 1: List of symbols

Symbol	Definition	Symbol	Definition
Alm	Almandine	Pyr	Pyrophanite
Adr	Andradite	Qtz	Quartz
Ann	Annite	RHOMOX	Rhombohedral oxide
Bt	Biotite	Rt	Rutile
Ccp	Chalcopyrite	Sil	Sillimanite
Gk	Geikielite	Sps	Spessartine
Grs	Grossular	St	Staurolite
Grt	Garnet	Usp	Ulvöspinel
Hem	Hematite	Zrn	Zircon
Ilm	Ilmenite		
Ky	Kyanite	*a*	Activity
Mag	Magnetite	*f*	Fugacity
Ms	Muscovite	*P*	Pressure
Phl	Phlogopite	*T*	Temperature
Po	Pyrrhotite	*X*	Mole fraction
Prp	Pyrope		
Py	Pyrite	OR	Rock oxidation ratio

All mineral symbols except Gk, Pyr, and RHOMOX from Kretz (1983).

and as inclusions within porphyroblasts. Rt crystals are typically rimmed or partially replaced by RHOMOX. It is unclear if these rim or replacement textures developed during prograde metamorphism or if they are retrograde. Additional Rt parageneses that are almost certainly retrograde are described below.

Some samples contain small amounts ($< \sim 1$ vol. %) of sulfides. Pyrite (Py), pyrrhotite (Po), and chalcopyrite (Ccp) crystals are found mainly in the rock matrix and much less commonly as inclusions within porphyroblasts. Crystals range from anhedral to euhedral and most are between 5 and 1000 μm in diameter. Ccp, Po, and Ni-sulfide are also found as tiny rounded 'droplets' within some Py. Evidence for some low-temperature supergene alteration of sulfides to Hem and limonite is present in most samples. Because supergene reactions may have modified the prograde sulfide assemblages (e.g. alteration of Po to Py), interpretation of metamorphic sulfide assemblages is somewhat hazardous.

Retrogression of Fe–Ti oxide phases

Small, Ilm-rich ($X_{Ilm} > \sim 0{\cdot}85$) RHOMOX $\pm$ Rt grains are commonly found (1) along cleavages and margins of biotite and, more rarely, muscovite crystals, and (2) in contact with and as partial rims around Mag grains. This Ilm $\pm$ Rt probably formed from retrograde Ti release

Table 2: Prograde mineral assemblages

Sample	Grt	Ky	Sil	RHOMOX	Mag	Py	Po	Ccp
36A	X			X	X	X		X
37C-2	X	X	X	X	X	X		
38A	X	X	X	X	X	X		X
39B	X	X	X	X	X		X	X
40A	X	X		X	X			
41C	X	X	X	X	X	X		
42A	X	X	X	X	X	X	X	
45A	X			X	X	X		
46B	X	X	?	X			X	X
47A-1	X	X	X	X	X			
48E	X	X	X	X	X			
49A	X			X	X	X		X
50B	X			X	X			
51B	X	X	X	X	X		X	X
52C	X			X	X		X	
54A	X	X	X	X	X			
55A	X	X	X	X	X	X		X
56A		X	X	X	X	X		X
57B	X	X	X	X	X		X	X
58A	X	X	X	X	X	X		
59A	X			X	X	X		
60A	X		X	X	X	X		
61B	X	X	X	X	X			X
62A	X	X	X	X			X	X
63A-2	X	X	X	X	X			
64B-2	X	X	X	X	X			
65A	X	X		X	X	X		
66A	X	X	X	X	X	X	X	
67A	X	X		X	X			
68A	X	X	?	X	X	X		X
69B	X	X		X	X	X		
70A	X	X		X	X	X		
71A	X	X	X	X	X		X	X
Chin11*	X	X	X	X	X	n.r.	n.r.	n.r.

All samples contain quartz, plagioclase, biotite, and muscovite. Sulfide assemblages not listed if strong limonite alteration present. n.r., not reported; ?, possible trace.
*Sample 11 of Chinner (1960).

from micas and Mag (e.g. Ague & Brimhall, 1988). The small Usp contents of the Mag grains probably reflect, at least in part, such retrograde Ti loss. It is unclear if retrograde Ilm nucleated and grew during cooling, or if pre-existing prograde metamorphic grains were compositionally modified during cooling.

Nearby matrix RHOMOX are largely pseudomorphed by fine-grained assemblages containing variable amounts of Rt, Ti-rich Ilm, Ti-poor Hem, and, rarely, titanite. These pseudomorphs are inferred to have originally been prograde crystals because the pseudomorphic replacement has generally preserved relict exsolution textures characteristic of cooling from high T. Fe_2O_3–$FeTiO_3$ phase relations predict that at T below $\sim$500°C, Ti-poor Hem and Ti-rich Ilm should coexist (e.g. Burton, 1991). Thus, the pseudomorphed RHOMOX probably comprise retrograde minerals that may have equilibrated to some degree with nearby retrograde Ilm $\pm$ Rt associated with micas and Mag. RHOMOX grains that are far from micas and Mag or that are preserved as inclusions within garnet, aluminosilicate, or tourmaline porphyroblasts are typically not pseudomorphed.

PRESSURE AND TEMPERATURE

P–T estimates for selected samples were computed with the TWEEQU program of Berman (1991) using the program's default thermodynamic data and activity models. Mole fractions were computed using version 0·95 of the CMP program available at the TWEEQU Web site (www.gis.nrcan.gc.ca/twq.html). The mole fraction of hydroxyl in micas was adjusted to include F and Cl substitution for OH (e.g. Ague & Brimhall, 1988; McMullin *et al.*, 1991). We calculated simultaneous solutions of: (I) the garnet–biotite Fe–Mg exchange (GARB; Alm + Phl = Py + Ann) and the SGAM reactions of McMullin *et al.* (1991; Alm + Ms = Ann + 2 Sil + Qtz, Prp + Ms = Phl + 2 Sil + Qtz); or (II) GARB and GRAIL (Alm + 3 Rt = Sil + 2 Qtz + 3 Ilm). Method (II) was applied to sample 62A, which contains rutile that appears not to be retrogressed (see above). Reactions involving grossular in garnet were not used because grossular contents are generally small and subject to significant uncertainties stemming from estimated andradite contents.

Results cluster in the sillimanite field (Fig. 3), averaging 657°C and 5·7 kbar; we used 660°C and 5·7 kbar to calculate fluid composition herein. T was also estimated using GARB at 5·7 kbar for five samples that lack aluminosilicate minerals (36A, 45A, 49A, 50B, 52C). The average T of 668°C agrees with the simultaneous *P–T* estimates of Fig. 3. Because larger garnet grains preserve bell-shaped Mn growth zoning profiles, the temperature–time evolution of these rocks was insufficient to cause complete diffusional equilibration of cations in garnet. Our *P–T* results are fully consistent with those of McLellan (1985).

REACTIONS

A fundamental conclusion of Chinner (1960) was that, for any given sample, silicates and oxides reacted together

Table 3: Rhombohedral oxide compositions

Sample	Type*	Ti	Al	Cr	Fe^{3+}	V	Fe^{2+}	Mn	Mg	Zn	Total	X_{Ilm}	X_{Hem}	X_{Gk}	X_{Pyr}
36A	M	0·735	0·005	0·007	2·505	0·012	0·715	0·018	0·001	0·002	100·00	0·360	0·630	tr.	0·009
37C-2	GS	1·730	0·001	0·004	0·522	0·009	1·692	0·030	0·009	0·001	99·26	0·849	0·131	0·005	0·015
38A	M	1·292	0·002	0·006	1·395	0·014	1·278	0·007	0·005	0·001	99·97	0·643	0·351	0·003	0·004
39B	M	1·791	0·002	0·005	0·405	0·005	1·737	0·043	0·010	0·002	99·11	0·872	0·102	0·005	0·022
40A	IG	1·298	0·006	n.d.	1·397	n.d.	1·257	0·020	0·022	n.d.	99·30	0·630	0·350	0·011	0·010
40A	RM	1·753	0·002	n.d.	0·493	n.d.	1·736	0·010	0·006	n.d.	98·99	0·868	0·123	0·003	0·005
41C	IG	1·016	0·002	0·002	1·958	0·006	0·996	0·017	0·001	0·002	99·43	0·500	0·491	tr.	0·009
42A	IG	0·596	0·010	0·004	2·786	0·007	0·573	0·019	0·002	0·002	101·48	0·289	0·700	0·001	0·010
45A	M	0·883	0·010	0·003	2·211	0·010	0·864	0·012	0·004	0·003	98·84	0·436	0·556	0·002	0·006
46B	IG	1·940	0·007	0·001	0·112	tr.	1·855	0·080	0·004	0·001	99·53	0·930	0·028	0·002	0·040
47A-1	IG	0·915	0·006	n.d.	2·164	n.d.	0·878	0·032	0·005	n.d.	99·03	0·439	0·542	0·003	0·016
47A-1	RM	1·941	0·002	n.d.	0·115	n.d.	1·867	0·073	0·002	n.d.	97·38	0·934	0·029	0·001	0·036
48E	IG	0·643	0·009	0·008	2·686	0·012	0·625	0·009	0·007	0·002	99·30	0·316	0·676	0·004	0·004
49A	M	0·800	0·005	tr.	2·385	0·008	0·686	0·112	0·002	0·001	100·58	0·345	0·598	0·001	0·056
50B	IG	0·628	0·003	0·002	2·734	0·005	0·585	0·041	tr.	0·002	100·33	0·294	0·685	tr.	0·020
51B	IG	1·015	0·002	0·002	1·956	0·009	0·997	0·017	tr.	0·002	99·99	0·501	0·491	tr.	0·008
52C	M	1·592	0·001	0·004	0·805	0·008	1·555	0·035	0·001	0·001	100·00	0·780	0·202	tr.	0·018
54A	IGT	0·802	0·005	0·004	2·377	0·010	0·791	0·009	0·001	0·002	100·97	0·398	0·597	tr.	0·005
55A	IGK	0·803	0·007	0·003	2·375	0·009	0·794	0·008	tr.	0·001	101·18	0·399	0·597	tr.	0·004
56A	IK	0·866	0·009	0·004	2·247	0·008	0·852	0·013	0·001	0·001	100·84	0·428	0·565	tr.	0·006
57B	M	0·835	0·004	0·002	2·312	0·012	0·826	0·008	0·001	0·001	101·12	0·415	0·581	tr.	0·004
57B	M	1·378	0·001	0·002	1·235	0·007	1·359	0·016	0·002	0·001	100·81	0·682	0·309	0·001	0·008
58A	M	0·970	0·004	0·010	2·034	0·012	0·960	0·008	0·001	0·001	100·00	0·484	0·512	tr.	0·004
58A	RM	1·734	tr.	0·006	0·521	0·006	1·706	0·023	0·002	0·003	99·92	0·857	0·131	0·001	0·011
59A	IG	0·869	0·002	0·002	2·252	0·005	0·846	0·019	0·003	0·002	100·28	0·425	0·564	0·002	0·009
60A	IG	0·738	0·002	0·005	2·507	0·010	0·720	0·017	0·001	tr.	99·73	0·362	0·629	tr.	0·008
61B	IGi	0·822	0·002	0·019	2·321	0·013	0·795	0·026	tr.	0·001	100·29	0·401	0·585	tr.	0·013
61B	IG	1·682	0·001	0·002	0·633	0·001	1·629	0·018	0·032	0·003	100·68	0·817	0·158	0·016	0·009
61B	ISM	1·782	0·001	0·002	0·431	0·004	1·767	0·008	0·006	0·001	100·10	0·885	0·108	0·003	0·004
62A	IG	1·957	tr.	0·001	0·083	0·002	1·904	0·050	0·002	tr.	100·35	0·953	0·021	0·001	0·025
63A-2	IG	1·007	0·000	0·001	1·977	0·004	0·956	0·048	0·003	tr.	100·05	0·479	0·495	0·002	0·024
64B-2	IG	0·911	0·004	0·001	2·167	0·005	0·886	0·023	0·002	tr.	99·75	0·445	0·543	0·001	0·011
65A	IG	0·932	0·006	0·006	2·115	0·008	0·922	0·009	0·001	tr.	99·85	0·464	0·531	tr.	0·005
66A	IGi	1·395	0·001	0·002	1·201	0·006	1·354	0·039	0·002	0·001	100·40	0·679	0·301	0·001	0·019
66A	IG	1·711	0·001	0·002	0·572	0·002	1·644	0·033	0·032	0·002	99·87	0·824	0·143	0·016	0·017
66A	ISM	1·701	0·001	0·004	0·589	0·005	1·670	0·025	0·005	0·001	100·12	0·837	0·148	0·002	0·013
66A	IK	1·738	0·002	0·002	0·518	0·003	1·703	0·017	0·016	0·002	99·69	0·854	0·130	0·008	0·009
66A	IK	1·661	0·003	0·002	0·669	0·004	1·614	0·016	0·030	0·001	98·80	0·809	0·168	0·015	0·008
67A	M	0·761	0·004	0·002	2·465	0·006	0·716	0·042	0·002	0·001	100·65	0·360	0·618	0·001	0·021
68A	M	1·097	0·005	0·004	1·787	0·010	1·089	0·006	tr.	0·002	100·12	0·548	0·449	tr.	0·003
68A	IG	1·325	0·001	0·006	1·334	0·010	1·295	0·026	0·002	0·002	99·73	0·651	0·335	0·001	0·013
68A	PKSt	1·829	tr.	0·005	0·331	0·006	1·796	0·025	0·005	0·003	100·07	0·902	0·083	0·003	0·013
69B	IK	0·622	tr.	0·004	2·740	0·012	0·602	0·012	tr.	0·008	101·09	0·306	0·688	tr.	0·006
70A	IK	0·922	0·006	0·004	2·136	0·010	0·906	0·015	tr.	0·001	100·12	0·456	0·537	tr.	0·008
71A	IG	1·726	0·001	0·002	0·544	0·002	1·702	0·011	0·012	0·001	100·24	0·852	0·136	0·006	0·006
71A	ISM	1·820	tr.	0·002	0·358	0·001	1·787	0·018	0·014	tr.	100·34	0·894	0·090	0·007	0·009
Chin11†	—	0·516	n.d.	n.d.	2·968	n.d.	0·516	n.d.	n.d.	n.d.	98·59	0·258	0·742	n.d.	n.d.

Six oxygen formula basis. n.d., not determined; tr., trace (<0·001). Fe^{2+}, Fe^{3+} calculated based on stoichiometry. Total is total weight percent incorporating calculated FeO and Fe_2O_3.
*GS, at garnet–sillimanite contact; IG, inclusions in garnet rim; IGi; inclusions in garnet interior; IGK, inclusions in garnet and kyanite; IGT, inclusions in garnet and tourmaline; IK, inclusions in kyanite; ISM, inclusions in sillimanite–muscovite aggregates; M, matrix grain; PKSt; at contact of plagioclase and post-sillimanite kyanite and staurolite; RM, retrograde grain in matrix.
†From Chinner (1960).

Table 4: Magnetite (Mag) and rutile (Rt) compositions

Sample	Phase	Type*	Ti	Al	Cr	Fe^{3+}	V	Fe^{2+}	Mn	Mg	Zn	Total	X_{Mag}
62A	Rt	IG	1·954	tr.	0·002	0·053	0·002	—	0·002	tr.	tr.	99·69	—
37C-2	Mag	M	0·030	0·017	0·002	1·919	0·003	1·026	tr.	0·003	0·001	99·71	0·959
39B	Mag	M	0·003	0·023	0·004	1·963	0·005	1·002	0·001	0·001	tr.	100·47	0·981
40A	Mag	IG	0·045	0·012	n.d.	1·898	n.d.	1·042	0·002	0·001	n.d.	100·29	0·949
40A	Mag	M	0·041	0·005	n.d.	1·914	n.d.	1·040	tr.	0·001	n.d.	99·66	0·957
41C	Mag	M	0·004	0·008	0·002	1·974	0·007	0·994	0·010	tr.	0·001	99·60	0·987
52C	Mag	M	0·005	0·011	0·001	1·971	0·006	1·004	tr.	tr.	0·001	101·20	0·986
54A	Mag	M	0·002	0·008	0·001	1·983	0·004	1·002	tr.	tr.	tr.	100·39	0·992
56A	Mag	M	0·002	0·009	0·001	1·981	0·004	1·002	tr.	tr.	tr.	100·09	0·991
61B	Mag	M	tr.	0·006	0·001	1·987	0·005	1·000	tr.	tr.	0·001	100·36	0·994
66A	Mag	M	0·001	0·005	0·001	1·989	0·004	0·999	tr.	tr.	0·001	100·30	0·994
71A	Mag	IG	0·001	0·018	0·003	1·970	0·006	1·001	tr.	tr.	tr.	100·19	0·985
71A	Mag	M	0·003	0·017	0·001	1·974	0·003	1·003	tr.	tr.	tr.	100·91	0·987

Four oxygen formula basis. n.d., not determined; tr., trace (<0·001). Magnetite Fe^{2+}, Fe^{3+} calculated based on stoichiometry. All Fe as Fe^{3+} for rutile. Total is total weight percent. Total incorporates calculated FeO and Fe_2O_3 in magnetite.
*IG, inclusions in garnet; M, matrix grains.

as part of a thermodynamic system. The primary reaction that we used to estimate f_{O_2} involves both silicates and magnetite

$$4Qtz + 2Mag + 2Sil = O_2 + 2Alm. \quad (1)$$

The main advantages of this reaction are that (1) nonideal activity corrections for Alm and Mag are well constrained for the compositional ranges of interest, and (2) Qtz and aluminosilicates are essentially pure phases. For rocks lacking aluminosilicate minerals or garnet we used

$$3Qtz + 2Mag + Ms = O_2 + Ann + Alm \quad (2)$$

$$2Qtz + 2Mag + 2Ms = O_2 + 2Ann + 2Sil. \quad (3)$$

We also considered the hematite analogs of reactions (1)–(3):

$$8Qtz + 6Hem + 4Sil = 3O_2 + 4Alm \quad (4)$$

$$6Qtz + 6Hem + 2Ms = 3O_2 + 2Ann + 2Alm \quad (5)$$

$$4Qtz + 6Hem + 4Ms = 3O_2 + 4Ann + 4Sil. \quad (6)$$

However, these reactions are complicated by uncertain activity–composition relations for RHOMOX (see below). This uncertainty is particularly problematic for the Mag–Hem reaction ($6Hem = 4Mag + O_2$) because f_{O_2} depends on the sixth power of the Hem activity. Thus, we do not consider this reaction further.

Given an estimate of the f_{O_2}, f_{S_2} was estimated using

$$2O_2 + 3Py = Mag + 3S_2 \quad (7)$$

for Py-bearing assemblages, and

$$2O_2 + 3Po = Mag + 1{\cdot}5S_2 \quad (8)$$

for Po-bearing ones. For samples that lack Mag and Py, we used the reaction $3O_2 + 4Po = 2Hem + 2S_2$.

The f_{HF}/f_{H_2O} estimates used measured biotite compositions (Table 5) following Zhu & Sverjensky (1992).

The $\log_{10}(a_{Mg^{2+}}/a_{Fe^{2+}})$ and $\log_{10}(a_{Mn^{2+}}/a_{Fe^{2+}})$ for the fluid were estimated with

$$Fe^{2+} + 1/3Prp = Mg^{2+} + 1/3Alm \quad (9)$$

and

$$Fe^{2+} + 1/3Sps = Mn^{2+} + 1/3Alm. \quad (10)$$

Calculation of $\log_{10}K$ for reaction (9) involves a slight extrapolation of fluid species thermodynamic data beyond the recommended maximum P of 5 kbar (Shock *et al.*, 1997), but we emphasize that we are concerned with regional *gradients* in fluid composition that are independent of log K, not absolute values. Because thermodynamic data for Sps are lacking, we plot $\log_{10}(a_{Mn^{2+}}/a_{Fe^{2+}}) - \log_{10}K$ for reaction (10).

ACTIVITY–COMPOSITION RELATIONS AND THERMODYNAMIC DATA

We used the activity model of Ghiorso (1990) for RHOMOX. However, Evans & Scaillet (1997) showed that

Table 5: Biotite (Bt) and muscovite (Ms) compositions

Sample	Phase	Si	Ti	Al^{iv}	Al^{vi}	Fe^{T}	Mn	Mg	Ba	Na	K	F	Cl	Total
36A	Bt	2·768	0·121	1·232	0·357	1·218	0·010	1·163	0·008	0·028	0·850	0·060	0·003	96·12
45A	Bt	2·767	0·133	1·233	0·321	1·288	0·018	1·105	0·007	0·027	0·878	0·082	0·001	95·76
46B	Bt	2·751	0·118	1·249	0·381	1·313	0·008	1·049	0·009	0·049	0·829	0·108	0·003	95·94
49A	Bt	2·771	0·128	1·230	0·340	1·289	0·035	1·064	0·008	0·016	0·892	0·068	0·001	95·87
50B	Bt	2·759	0·135	1·242	0·330	1·228	0·008	1·155	0·008	0·031	0·883	0·092	tr.	95·48
52C	Bt	2·756	0·131	1·244	0·337	1·392	0·009	0·993	0·006	0·027	0·883	0·068	0·001	95·61
54A	Bt	2·733	0·107	1·267	0·370	1·247	0·004	1·166	0·004	0·054	0·832	0·064	tr.	96·11
55A	Bt	2·741	0·121	1·259	0·378	1·182	0·004	1·185	0·006	0·040	0·850	0·081	tr.	95·68
56A	Bt	2·735	0·120	1·265	0·381	1·212	0·006	1·150	0·006	0·038	0·855	0·052	tr.	96·11
57B	Bt	2·736	0·151	1·264	0·339	1·292	0·004	1·062	0·006	0·031	0·883	0·096	tr.	95·96
61B	Bt	2·742	0·097	1·258	0·388	1·265	0·002	1·133	0·006	0·042	0·853	0·075	0·005	95·48
62A	Bt	2·756	0·098	1·244	0·392	1·232	0·003	1·148	0·005	0·031	0·868	0·173	0·003	95·88
66A	Bt	2·732	0·135	1·268	0·367	1·246	0·003	1·100	0·009	0·047	0·864	0·094	tr.	95·80
70A	Bt	2·737	0·126	1·263	0·369	1·185	0·004	1·186	0·006	0·043	0·848	0·074	0·001	95·27
71A	Bt	2·730	0·118	1·270	0·416	1·337	0·001	1·008	0·005	0·046	0·804	0·077	0·001	95·98
Chin11*	Bt	2·696	0·060	1·304	0·558	0·879	0·015	1·378	n.d.	0·076	0·769	tr.	n.d.	95·13
36A	Ms	3·100	0·055	0·900	1·727	0·192	0·001	0·074	0·009	0·125	0·824	0·022	tr.	94·65
45A	Ms	3·108	0·048	0·892	1·709	0·216	0·001	0·085	0·006	0·094	0·864	0·011	tr.	94·19
46B	Ms	3·102	0·060	0·898	1·769	0·120	tr.	0·082	0·005	0·110	0·828	0·024	tr.	94·35
49A	Ms	3·155	0·042	0·845	1·666	0·234	0·001	0·120	0·014	0·067	0·876	0·019	0·001	94·89
50B	Ms	3·122	0·039	0·878	1·730	0·188	0·001	0·090	0·008	0·116	0·839	0·024	tr.	94·52
52C	Ms	3·127	0·040	0·873	1·729	0·192	tr.	0·085	0·009	0·124	0·830	0·017	tr.	94·00
54A	Ms	3·107	0·041	0·893	1·758	0·163	0·001	0·076	0·009	0·183	0·776	0·011	tr.	95·23
55A	Ms	3·097	0·043	0·903	1·743	0·183	0·001	0·081	0·009	0·146	0·809	0·026	tr.	95·10
56A	Ms	3·093	0·045	0·907	1·730	0·199	0·001	0·085	0·010	0·143	0·804	0·011	tr.	94·58
57B	Ms	3·098	0·052	0·902	1·724	0·190	0·001	0·082	0·010	0·127	0·833	0·011	tr.	94·84
61B	Ms	3·109	0·039	0·891	1·745	0·189	tr.	0·080	0·006	0·155	0·795	0·009	tr.	94·73
62A	Ms	3·096	0·055	0·904	1·790	0·101	0·001	0·076	0·008	0·136	0·808	0·009	tr.	94·85
66A	Ms	3·095	0·043	0·905	1·747	0·183	tr.	0·079	0·010	0·133	0·817	0·013	tr.	94·30
70A	Ms	3·108	0·045	0·892	1·719	0·208	0·001	0·088	0·007	0·139	0·808	0·021	tr.	94·95
71A	Ms	3·104	0·051	0·896	1·750	0·167	tr.	0·077	0·008	0·129	0·810	0·011	0·001	94·39
Chin11*	Ms	3·077	0·028	0·923	1·738	0·205	0·014	0·117	n.d.	0·160	0·765	n.d.	n.d.	94·34

Eleven oxygen formula basis. n.d., not determined; tr., trace (<0·001). All Fe as Fe^{2+}. Total is total weight percent. Oxygen equivalents of the fluorine and chlorine atoms have not been subtracted from the weight percent totals.
*Sample 11 of Chinner (1960).

current RHOMOX models overestimate f_{O_2} for highly oxidized Mt Pinatubo dacites (see below).

Retrograde Ti loss commonly alters the bulk composition of Mag. However, because 'peak' metamorphic T was $< \sim 700°C$, the expected X_{Mag} for spinel coexisting with the measured RHOMOX compositions would have been large and between about 0·80 and 1·0 (Andersen & Lindsley, 1988; Ghiorso & Sack, 1991). The Ti-poor Mag inclusions in garnet (Table 4) support this idea because they should have been shielded from retrograde equilibration with matrix phases and thus preserve prograde compositions. For T of 650–700°C in the Fe_3O_4–Fe_2TiO_4 system, the appropriate Mag activities for our samples are between about 0·8 and 1·0 (Andersen & Lindsley, 1988; Ghiorso & Sack, 1991); we used a very conservative range between 0·75 and 1·0 herein. Other components such as $MgAl_2O_4$ could also have affected Mag activity, but they are present in only trace amounts (Table 4); their concentrations are generally significant only at much higher T (Ghiorso & Sack, 1991).

Po that coexists with Py in the Fe–S system deviates from ideal FeS by as much as $Fe_{0·875}S$ at high T. However, natural high-T Po compositions commonly equilibrate down to very low T, at which many complex phase

Table 6: Garnet compositions

Sample	Si	Al^{iv}	Σ^{iv}	Al^{vi}	Ti	Fe^{3+}	Fe^{2+}	Mn	Mg	Ca	Σ^{viii}	Total	X_{Alm}	X_{Prp}	X_{Sps}	X_{Grs}	X_{Adr}
36A	3·005	0·000	3·005	1·967	0·001	0·033	1·888	0·584	0·297	0·220	2·989	99·65	0·631	0·099	0·195	0·057	0·017
37C-2	2·988	0·012	3·000	1·973	tr.	0·027	2·180	0·288	0·410	0·128	3·006	100·33	0·725	0·136	0·096	0·029	0·013
38A	3·000	0·000	3·000	1·955	tr.	0·045	2·236	0·206	0·388	0·169	2·999	100·12	0·745	0·129	0·069	0·034	0·022
39B	2·994	0·006	3·000	1·965	0·001	0·034	2·199	0·201	0·416	0·186	3·002	99·83	0·732	0·139	0·067	0·044	0·018
40A	2·961	0·039	3·000	1·923	0·001	0·076	2·218	0·052	0·479	0·270	3·019	99·75	0·735	0·159	0·017	0·051	0·038
41C	3·001	0·000	3·001	1·935	tr.	0·065	2·134	0·311	0·410	0·143	2·997	99·69	0·712	0·137	0·104	0·015	0·033
42A	2·992	0·008	3·000	1·966	0·001	0·033	2·098	0·353	0·398	0·155	3·004	100·10	0·698	0·132	0·117	0·035	0·017
45A	3·022	0·000	3·022	1·951	tr.	0·049	1·955	0·462	0·334	0·204	2·955	99·13	0·662	0·113	0·156	0·044	0·025
46B	2·996	0·004	3·000	1·983	tr.	0·017	2·314	0·096	0·406	0·187	3·002	99·61	0·771	0·135	0·032	0·054	0·009
47A1	2·982	0·018	3·000	1·948	tr.	0·053	2·108	0·312	0·438	0·151	3·009	100·72	0·701	0·146	0·104	0·024	0·026
48E	3·000	0·000	3·000	1·978	tr.	0·022	2·192	0·263	0·408	0·135	2·999	99·82	0·731	0·136	0·088	0·034	0·011
49A	2·989	0·011	3·000	1·960	tr.	0·041	1·841	0·561	0·353	0·250	3·005	99·97	0·613	0·117	0·187	0·063	0·020
50B	2·986	0·014	3·000	1·936	0·001	0·063	2·039	0·306	0·422	0·240	3·006	99·90	0·678	0·140	0·102	0·048	0·032
51B	3·005	0·000	3·005	1·982	tr.	0·018	2·241	0·199	0·413	0·138	2·990	100·00	0·749	0·138	0·066	0·037	0·009
52C	2·998	0·002	3·000	1·933	tr.	0·067	2·068	0·347	0·384	0·201	3·001	100·31	0·689	0·128	0·116	0·034	0·034
54A	2·995	0·005	3·000	1·964	tr.	0·036	2·156	0·289	0·415	0·142	3·003	100·39	0·718	0·138	0·096	0·029	0·018
55A	2·990	0·010	3·000	1·953	0·001	0·046	2·067	0·326	0·423	0·188	3·005	99·83	0·688	0·141	0·109	0·039	0·024
57B	3·004	0·000	3·004	1·969	tr.	0·031	2·162	0·268	0·425	0·138	2·993	100·07	0·722	0·142	0·089	0·031	0·016
58A	2·993	0·007	3·000	1·958	tr.	0·042	2·142	0·298	0·415	0·148	3·003	99·91	0·713	0·138	0·099	0·028	0·021
59A	2·990	0·010	3·000	1·962	tr.	0·038	2·045	0·441	0·403	0·116	3·005	99·89	0·681	0·134	0·147	0·019	0·019
60A	2·990	0·010	3·000	1·961	tr.	0·039	2·172	0·273	0·401	0·159	3·005	99·87	0·723	0·134	0·091	0·033	0·019
61B	3·005	0·000	3·005	1·971	tr.	0·029	2·323	0·106	0·391	0·169	2·990	99·83	0·777	0·131	0·036	0·042	0·015
62A	3·002	0·000	3·002	1·964	0·001	0·036	2·249	0·075	0·396	0·275	2·995	100·16	0·751	0·132	0·025	0·074	0·018
63A-2	2·996	0·004	3·000	1·979	0·001	0·020	2·140	0·274	0·406	0·182	3·001	99·99	0·713	0·135	0·091	0·050	0·011
64B-2	2·993	0·007	3·000	1·968	0·001	0·031	2·237	0·176	0·425	0·166	3·003	99·97	0·745	0·142	0·058	0·039	0·016
65A	3·007	0·000	3·007	1·959	0·002	0·038	2·189	0·163	0·412	0·222	2·985	99·82	0·733	0·138	0·054	0·054	0·020
66A Int.*	3·010	0·000	3·010	1·910	0·001	0·090	1·936	0·421	0·228	0·394	2·979	99·95	0·650	0·076	0·141	0·087	0·045
66A	2·975	0·025	3·000	1·931	tr.	0·069	2·139	0·195	0·412	0·267	3·013	100·29	0·710	0·137	0·065	0·054	0·034
67A	2·991	0·009	3·000	1·945	tr.	0·055	1·953	0·312	0·472	0·267	3·004	100·09	0·650	0·157	0·104	0·061	0·028
68A	2·994	0·006	3·000	1·963	0·001	0·036	2·222	0·219	0·390	0·170	3·002	100·18	0·740	0·130	0·073	0·038	0·019
69B	2·993	0·007	3·000	1·965	tr.	0·035	2·165	0·314	0·412	0·112	3·003	100·03	0·721	0·137	0·105	0·020	0·018
70A	3·001	0·000	3·001	1·975	tr.	0·025	2·117	0·345	0·423	0·114	2·998	99·79	0·706	0·141	0·115	0·026	0·012
71A	2·991	0·009	3·000	1·976	0·001	0·023	2·324	0·129	0·394	0·158	3·004	99·99	0·774	0·131	0·043	0·040	0·012
Chin11†	3·041	0·000	3·041	1·902	0·007	0·055	1·615	0·427	0·786	0·141	2·969	99·52	0·562	0·120	0·272	0·019	0·027

Twelve oxygen formula basis. tr., trace (<0·001). Fe^{2+}, Fe^{3+} calculated based on stoichiometry. Total is total weight percent incorporating calculated FeO and Fe_2O_3.
*Garnet interior.
†Sample 11 of Chinner (1960). Mole fractions from Chinner (1960).

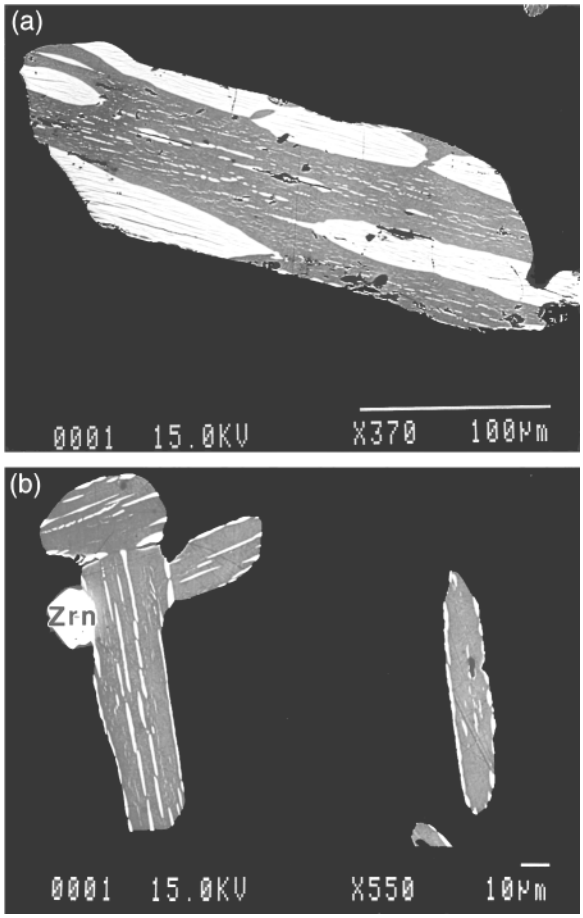

Fig. 2. Backscattered electron images of rhombohedral oxides (RHOMOX) included within interior (a) and rim (b) of garnet in sample 66A. RHOMOX inclusions are more ilmenite rich towards rim of garnet. Ilmenite-rich lamellae, dark gray; hematite-rich lamellae, light gray. Multiple sets of exsolution lamellae in (a) should be noted. Composition of hematite-rich domains in (a) (including fine ilmenite-rich lamellae): $X_{Ilm} = 0{\cdot}32$; $X_{Hem} = 0{\cdot}67$; $X_{Gk} = 3{\cdot}9 \times 10^{-4}$; $X_{Pyr} = 7{\cdot}8 \times 10^{-3}$. Ilmenite-rich domains in (a) (including fine hematite-rich lamellae): $X_{Ilm} = 0{\cdot}84$; $X_{Hem} = 0{\cdot}13$; $X_{Gk} = 1{\cdot}0 \times 10^{-3}$; $X_{Pyr} = 2{\cdot}3 \times 10^{-2}$. White, equant grain at left in (b) is zircon (Zrn).

transitions occur. In view of these retrograde complications, we make the simplification of setting the activity of Po to 1·0. This simplification introduces some error, but the activity corrections for even highly non-stoichiometric Po have minor impact on the resolution of the large variations in fugacities of interest here. Py is relatively pure and its activity was set to 1·0.

Activity coefficients for garnet components, Ann, and Ms were computed following Berman (1990), McMullin *et al.* (1991) and Chatterjee & Froese (1975), respectively.

Because the rocks are in the sillimanite zone and nearly all samples contain Sil, thermodynamic data for sillimanite were used in the calculations; use of Ky has little impact on the results. Reconnaissance analyses indicate that the aluminosilicate minerals are relatively

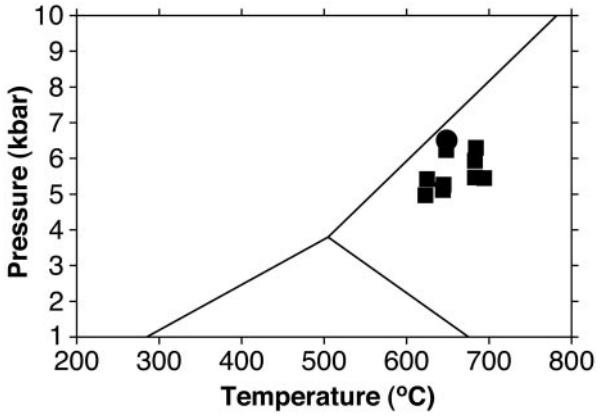

Fig. 3. Pressure–temperature estimates. ■, method (I); ●, method (II) (see text). Samples 46B, 54A, 55A, 57B, 61B, 62A, 66A, 70A, and 71A. Al_2SiO_5 phase relations from Berman (1988).

pure Al_2SiO_5 ($X_{Al_2SiO_5}$ >0·99) and thus can be modeled using unit activity. Qtz was assumed to be pure SiO_2.

Thermodynamic data for Mag and most silicate components were taken from Berman (1988). Data for Hem, Ann, Alm, and F-bearing micas were taken from Ghiorso (1990), McMullin *et al.* (1991), Berman (1990), and Zhu & Sverjensky (1992), respectively, and are internally consistent with Berman (1988). Results computed with these standard state properties are nearly identical to those computed using recently revised properties for Alm and Mag (Berman & Aranovich, 1996). For example, the two datasets yield f_{O_2} values for reaction (1), the main reaction we used to estimate f_{O_2}, that differ by only 0·04 log units. We used data from Johnson *et al.* (1992), as updated by Shock *et al.* (1997) and Sverjensky *et al.* (1997), for sulfide minerals, graphite, and most fluid species. Data for the gases CO, HF, and COS are not included in the Johnson *et al.* (1992) database and were thus taken from Robie *et al.* (1979), Stull & Prophet (1971), and Wagman *et al.* (1982), respectively.

Speciation calculations were carried out for C–O–H–S fluids composed of H_2O, H_2, CO_2, CO, CH_4, COS, S_2, SO_2, and H_2S. Fugacity and activity coefficients for H_2O and CO_2 were from Kerrick & Jacobs (1981), whereas the other fugacities were computed using the equations of Shi & Saxena (1992) assuming ideal mixing of non-ideal gas species. Solution of the non-linear system of speciation equations was carried out using standard procedures (e.g. Ferry & Baumgartner, 1987; Holloway, 1987).

FUGACITIES AND MINERAL CHEMISTRY

Oxygen fugacity

Results are given in terms of ΔQFM defined here as the difference, at 660°C and 5·7 kbar, between the $\log_{10} f_{O_2}$

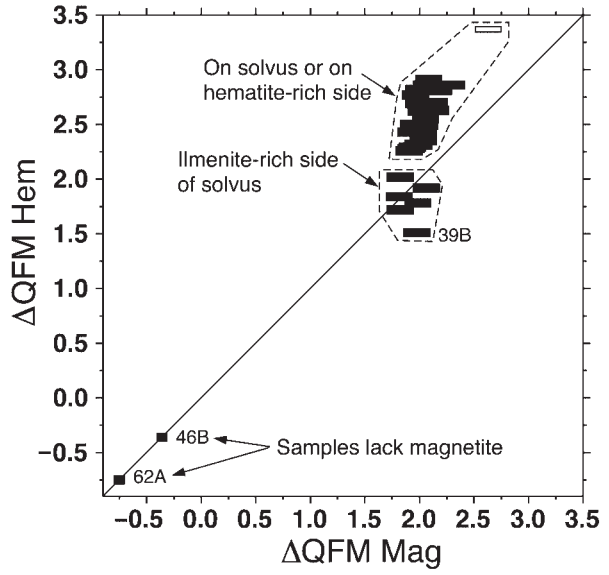

Fig. 4. ΔQFM computed using hematite-bearing reactions (ΔQFM Hem) vs ΔQFM computed using magnetite-bearing ones (ΔQFM Mag). Results obtained using reactions (1) and (4) for aluminosilicate + garnet-bearing assemblages, reactions (2) and (5) for aluminosilicate-free assemblages, and reactions (3) and (6) for garnet-free assemblages. When possible, ΔQFM Hem was estimated using compositions of RHOMOX grains included in garnet rims or in aluminosilicate minerals. For samples lacking RHOMOX inclusions in porphyroblasts, compositions of RHOMOX in the matrix as far removed as possible from micas were used (Table 3). Length of black bars corresponds to ΔQFM Mag calculated for the range in magnetite activities from 0·75 to 1·0 (see text). In this and other plots, analytical variability in Grt almandine content yields uncertainties in ΔQFM Mag of $\sim \pm 0{\cdot}03$ $\log_{10}$ units (not shown). ΔQFM Hem and ΔQFM Mag agree reasonably well for samples with RHOMOX compositions on the ilmenite-rich side of the ilmenite–hematite solvus (37C-2, 39B, 52C, 61B, 66A, 71A). High f_{O_2} sample 11 of Chinner (1960) denoted by open rectangle. Samples 46B and 62A lack magnetite, but are plotted on the 1:1 correlation line for comparison purposes.

for a sample and that for the quartz–fayalite–magnetite (QFM) buffer (QFM $\log_{10} f_{O_2} = -17{\cdot}46$). Because T–f_{O_2} trajectories for rocks are generally subparallel to that for QFM, use of ΔQFM notation largely removes uncertainties caused by errors in T estimates and, therefore, highlights real f_{O_2} variations between samples. Furthermore, the reactions used to estimate f_{O_2} are fairly insensitive to P variations, thus minimizing errors caused by errors in the P estimate.

ΔQFM values computed using Hem-bearing reactions (ΔQFM Hem) are plotted against the corresponding Mag-bearing reactions (ΔQFM Mag) in Fig. 4. Most rocks have ΔQFM Hem between $+1{\cdot}75$ and $+3{\cdot}0$ and ΔQFM Mag of $+1{\cdot}8$ to $+2{\cdot}3$. However, ΔQFM values for the Mag-free samples 46B and 62A are 2–3 orders of magnitude lower than those for the other rocks (ΔQFM $-0{\cdot}25$ to $-0{\cdot}75$; Fig. 4).

Closer inspection reveals that the ΔQFM Hem estimates are as much as $\sim$10 times greater than the ΔQFM Mag estimates. The six samples that do cluster near the 1:1 correlation line (37C-2, 39B, 52C, 61B, 66A, 71A) all have RHOMOX compositions that lie on the Ilm-rich side of the Hem–Ilm solvus. Agreement between ΔQFM Hem and ΔQFM Mag for these samples may be due to the fact that most experiments in the Fe_2O_3–$FeTiO_3$ system have used Ilm-rich compositions (see Ghiorso, 1990). Consequently, the activity–composition relations for Ilm-rich RHOMOX are probably reasonably well understood. We note that ΔQFM Hem for sample 39B, which plots somewhat farther from the 1:1 line than the other five samples, is based on the composition of matrix RHOMOX. The RHOMOX in this sample may have undergone some retrograde Ti gain by exchange with matrix phases during cooling (see above), and its ΔQFM Hem may be somewhat underestimated.

The samples that plot well above the 1:1 line have compositions that are either on the solvus or to the Hem-rich side (Fig. 4). Problems with current RHOMOX activity models near the solvus have been documented (Evans & Scaillet, 1997), and the Hem-rich side of the solvus remains to be fully explored experimentally. Consequently, the ΔQFM Hem values for these samples are inferred to be less reliable than those for Ilm-rich compositions. Furthermore, the RHOMOX in samples that plot well above the 1:1 line contain complex exsolution textures. It is possible that these grains originally straddled the solvus and were thus composed of two coexisting RHOMOX compositions at peak T. In this case, our 'integrated' compositions, which are averaged over all exsolution domains in RHOMOX grains, would be in error and could not be used in thermodynamic calculations. Resolution of the above issues requires a better understanding of phase relations among rhombohedral oxides.

To avoid problems with the thermodynamic treatment of RHOMOX, we focus on ΔQFM values computed using Mag-bearing reactions (Table 7). The two exceptions are samples 46B and 62A, which lack Mag and require ΔQFM estimates based on Hem-bearing reactions. Because these two samples contain Ilm-rich RHOMOX that lacks exsolution features, they should be treated reasonably well with the activity model and standard state thermodynamic data used herein.

The agreement between ΔQFM estimates made using reactions (1), (2), and (3) for Mag-bearing samples, or reactions (4), (5), and (6) for Mag-free samples (Table 7), indicates that the thermodynamic data and activity models employed are internally consistent.

Mineral chemistry

Prograde RHOMOX vary from $X_{Hem} \sim 0{\cdot}02$ to $\sim 0{\cdot}75$ (Table 3). X_{Hem} values for inferred retrograde RHOMOX

Table 7: Fugacity and rock compositions

Sample	ΔQFM(1)	ΔQFM(2)	ΔQFM(3)	FeO	Fe_2O_3	OR	$\Delta HF/H_2O$	Elevation (m)
36A		2·05–2·30					0·100	325
37C-2	1·86–2·11			7·2	3·00	31·6		440
38A	1·80–2·05							505
39B	1·85–2·10							405
40A	1·86–2·11							365
41C	1·91–2·16							445
42A	1·96–2·21							460
45A		1·93–2·18					0·266	263
46B	−0·36*	−0·34†	−0·33‡				0·417	315
47A1	1·92–2·17			7·3	3·49	35·4		370
48E	1·84–2·09							450
49A		1·96–2·21					0·194	390
50B		1·94–2·19					0·294	310
51B	1·78–2·03							340
52C		1·70–1·95					0·227	430
54A	1·89–2·14	1·87–2·12	1·84–2·09				0·136	480
55A	2·01–2·26	1·97–2·22	1·93–2·18	4·6	2·84	43·5	0·230	510
56A			1·82–2·07	8·0	4·41	39·7	0·047	385
57B	1·87–2·12	1·77–2·02	1·67–1·92				0·355	420
58A	1·91–2·16							460
59A	2·02–2·27							490
60A	1·87–2·12			6·6	3·77	40·9		490
61B	1·69–1·94	1·73–1·98	1·77–2·02	10·2	2·76	21·7	0·216	525
62A	−0·75*	−0·69†	−0·63‡	8·0	1·81	18·5	0·595	450
63A-2	1·91–2·16							410
64B-2	1·80–2·05			5·6	4·28	51·1		350
65A	1·85–2·10							370
66A	1·94–2·19	1·87–2·12	1·79–2·04	7·6	2·85	28·9	0·326	400
67A	2·17–2·42							450
68A	1·81–2·06							485
69B	1·87–2·12							495
70A	1·92–2·17	1·91–2·16	1·90–2·15	5·3	3·52	46·0	0·190	445
71A	1·70–1·95	1·68–1·93	1·66–1·91	5·2	2·23	32·4	0·279	385
Chin11§	2·51–2·76	2·56–2·81	2·60–2·85	3·7	12·01	74·8		

ΔQFM (1), ΔQFM (2), ΔQFM (3) computed using reactions (1), (2), and (3), respectively, except where noted otherwise. Range in values corresponds to the magnetite activity range 0·75–1·0. FeO and Fe_2O_3 are bulk-rock weight percents. OR, rock oxidation ratio. $\Delta HF/H_2O$ is the difference in $\log_{10}(f_{HF}/f_{H_2O})$ between the sample and $\log_{10}(f_{HF}/f_{H_2O})$ for a standard biotite having $X_{Mg} = 0{\cdot}5$ and $\log_{10}(X_F/X_{OH}) = -1{\cdot}5$ at 660°C and 5·7 kbar.
*Computed using reaction (4).
†Computed using reaction (5).
‡Computed using reaction (6).
§Sample 11 of Chinner (1960).

intergrown with micas are smaller than ∼0·15 and are significantly smaller than the X_{Hem} of crystals included in nearby porphyroblasts (Table 3).

'Felted mats' of Sil intergrown with micas and, in some cases, retrograde St or Ky commonly contain significant quantities of RHOMOX. These yield X_{Hem} values that are equal to or smaller than those for inclusions in porphyroblasts (Table 3). It is unclear if the smaller

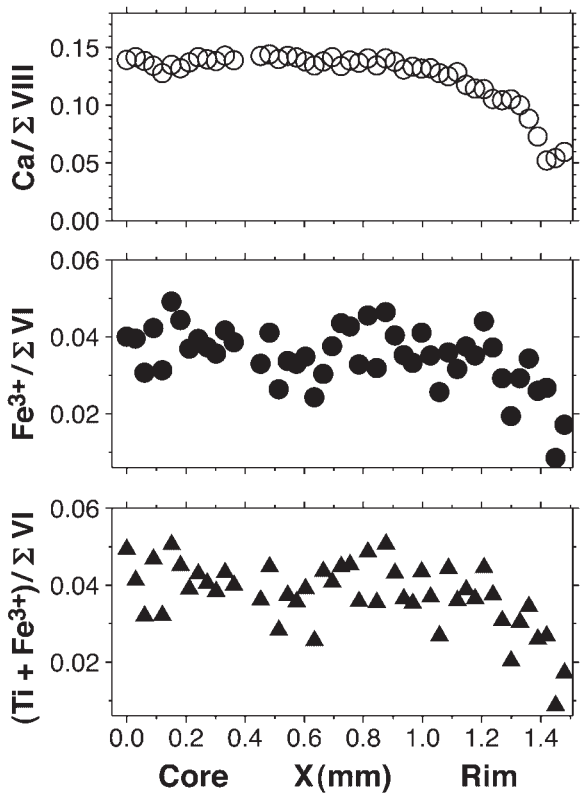

Fig. 5. Chemical traverses from core to rim across typical garnet in sample 66A. ΣVI and ΣVIII denote cation sums for six-fold and eight-fold coordinated sites, respectively.

values resulted from input of reducing fluid, retrogression, or both. Retrograde effects are difficult to rule out because the RHOMOX are closely intergrown with micas.

Samples 57B and 68A appear to have two coexisting prograde RHOMOX compositions that occur as discrete grains. Using the solvus diagram of Ghiorso (1990), compositions in 68A suggest a T near 680°C, in good agreement with the T estimates based on thermobarometry, whereas compositions in 57B are inconsistent with equilibration at a single T. The significance of these results is unclear given continuing uncertainties regarding T–activity–composition relations for RHOMOX.

Garnet Fe^{3+} is generally largest in cores and smallest in rims (Fig. 5). Fe^{3+} and Ti^{4+} decrease with Ca (Fig. 5), such that the ratio of grossular to andradite component remains fairly constant. Garnet Fe^{3+} contents are small and no correlation between ΔQFM and garnet Fe^{3+} is evident, consistent with Chinner (1960). The Fe^{3+} systematics are apparently sensitive mostly to crystal chemical factors and the availability of Ca, rather than f_{O_2}.

Garnet Mn content is in general positively correlated with rock Fe^{3+}/Fe^{2+} (Chinner, 1960), although not

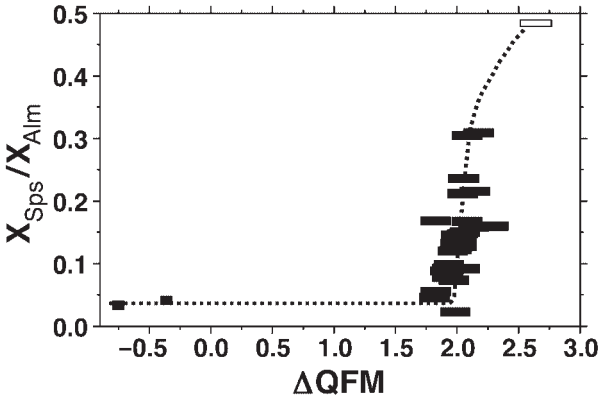

Fig. 6. Spessartine/almandine mole fraction ratio (X_{Sps}/X_{Alm}) vs ΔQFM. High f_{O_2} sample 11 of Chinner (1960) denoted by open rectangle.

necessarily with f_{O_2}. The X_{Sps}/X_{Alm} ratio is small for ΔQFM <0, whereas a wide range of X_{Sps}/X_{Alm} values seem compatible with ΔQFM of $\sim +2$ (Fig. 6). Sample 11 of Chinner (1960) is somewhat anomalous relative to our samples and has the largest X_{Sps}/X_{Alm} and f_{O_2} (Fig. 6). We note in this regard the possibility that the bulk garnet composition given by Chinner (1960) may be more Mn rich than the peak-T composition at garnet rims.

The X_{Mg}/X_{Fe^T} ratio for biotite changes little over the ΔQFM range between $-1{\cdot}0$ and $+2{\cdot}3$ (Fig. 7; Fe^T is all Fe as FeO). However, X_{Mg}/X_{Fe^T} increases at the largest ΔQFM, consistent with the expectation that higher f_{O_2} should favor more Mg-rich compositions (e.g. Wones & Eugster, 1965). The X_{Mg}/X_{Fe^T} of muscovite (Ms) decreases between ΔQFM $-1{\cdot}0$ and $+2{\cdot}3$, and then increases somewhat for higher ΔQFM (Fig. 7). Fe^{3+} is the dominant form of Fe in Glen Clova Ms (Chinner, 1960). Under reducing conditions, the total Fe content of Ms is relatively small because the amount of Fe^{3+} available is limited relative to more oxidized conditions. Consequently, X_{Mg}/X_{Fe^T} ratios for Ms in the low-f_{O_2} rocks are large. The slight increase in X_{Mg}/X_{Fe^T} above ΔQFM $+2$ reflects the stability of magnesian compositions at higher f_{O_2}.

Changes in RHOMOX inclusion compositions from core-to-rim in garnet

Some samples were examined in detail to determine if RHOMOX inclusion compositions changed from core to rim in garnets. This effort was hampered by the relatively small size and paucity of inclusions in many of the garnet crystals. None the less, RHOMOX included in the interiors of garnet porphyroblasts in samples 61B and 66A were measured to have significantly smaller X_{Ilm} than RHOMOX inclusions near

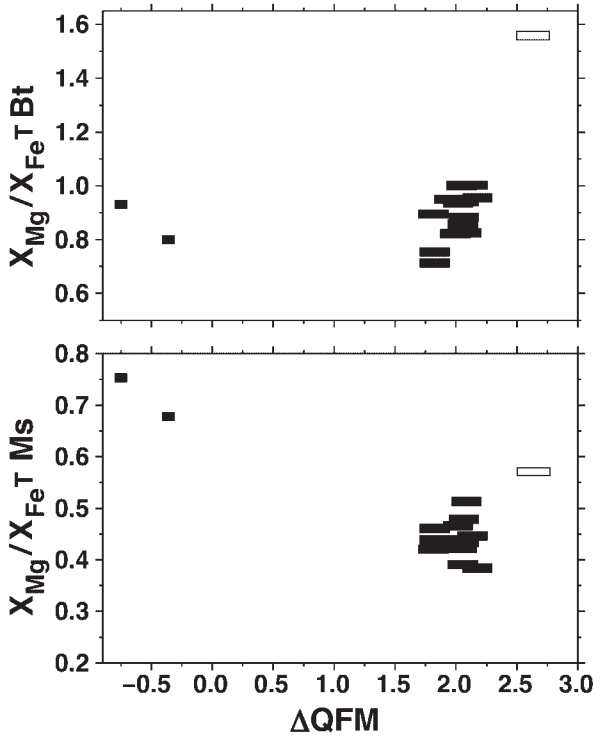

Fig. 7. Mg/Fe^{T} (all Fe as Fe^{2+}) mole fraction ratio vs ΔQFM for biotite (Bt; upper panel) and muscovite (Ms; lower panel). High f_{O_2} sample 11 of Chinner (1960) denoted by open rectangles.

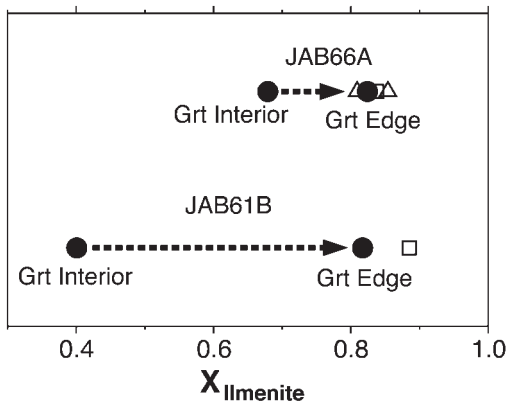

Fig. 8. Rhombohedral oxide (RHOMOX) ilmenite mole fractions for samples 61B and 66A. ●, RHOMOX inclusions in garnet; △, inclusions in kyanite rims; □, inclusions in sillimanite + muscovite aggregates. Generalized changes in RHOMOX compositions during garnet growth denoted by dashed arrows.

garnet rims, or those included within Sil + Ms aggregates and Ky rims (Figs 2 and 8; Table 3). One interpretation of this shift towards larger X_{Ilm} is that reducing fluids, either locally or externally derived, caused reduction of the mineral assemblage during garnet growth. Unfortunately, uncertainties in activity–composition relations for RHOMOX preclude full quantification of possible f_{O_2} changes recorded by the increases in X_{Ilm}, although calculations using the Ghiorso (1990) model suggest that drops in f_{O_2} as large as an order of magnitude occurred during garnet growth. Because RHOMOX compositions between the small X_{Ilm} values in Grt interiors and the large X_{Ilm} values in rims were not observed, any such reduction was probably rapid compared with the rate of Grt growth.

Relationships between f_{O_2} and f_{S_2}

Most sulfide-bearing samples record f_{S_2} at or slightly below the Py–Po buffer (Fig. 9). The average f_{S_2} of Py-bearing rocks is slightly higher than that for Po-bearing ones, consistent with thermodynamic predictions. The two samples with the smallest ΔQFM (46B, 62A) are the only ones that could have been in equilibrium with graphite. These record f_{S_2} values 2–3 orders of magnitude less than the other rocks (Fig. 9; see below).

REGIONAL VARIATIONS

Regional variations in f_{O_2}

Regional f_{O_2} profiles were constructed for the northwest, central, and southeast parts of the field area (Fig. 1). Because the fabric of the rocks is nearly horizontal, sample data were projected onto vertical sections such that the profiles are essentially perpendicular to the fabric. A small number of samples (46–49) are located between the northwest and central profile areas and are thus not shown in Figs 10 and 11.

ΔQFM for the northwestern and southeastern profiles shows no large variations as a function of elevation (Fig. 10a and c). The main feature of the central profile is the strong localized minimum in ΔQFM associated with sample 62A (Fig. 10b).

Regional variations in activities of Mg, Fe, and Mn species in solution

Surprisingly, the calculated $\log_{10}(a_{Mg^{2+}}/a_{Fe^{2+}})$ of the fluid varies little and shows no significant correlations with elevation or ΔQFM (Fig. 11). Nearly all values are within ±10% of the mean. Other related ratios, such as $\log_{10}(a_{MgCl^{+}}/a_{FeCl^{+}})$, would show exactly the same patterns of regional variation [of course, the absolute values would be different from $\log_{10}(a_{Mg^{2+}}/a_{Fe^{2+}})$]. These results strongly suggest that no large gradients in fluid Mg/Fe existed between layers. ΔQFM for all samples must have been low enough so that Fe^{2+} species were dominant, otherwise

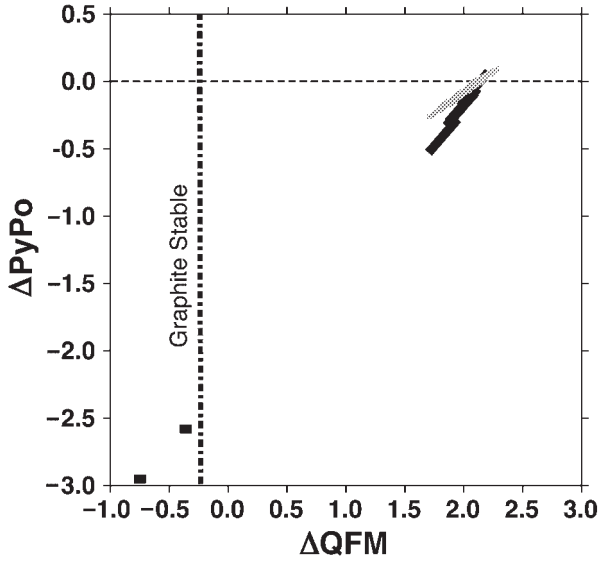

Fig. 9. ΔPyPo vs ΔQFM. ΔPyPo is the difference between $\log_{10} f_{S_2}$ for the sample and $\log_{10} f_{S_2}$ for the pyrite–pyrrhotite buffer at 660°C and 5·7 kbar. For rocks that contain magnetite (all those at ΔQFM above graphite stability), gray and black bars denote pyrite-bearing and pyrrhotite-bearing samples, respectively. Length of bars corresponds to ΔQFM calculated for the range in magnetite activities from 0·75 to 1·0 (see text). It should be noted that only the two magnetite-free, pyrrhotite-bearing samples (46B, 62A) fall within the stability field of graphite.

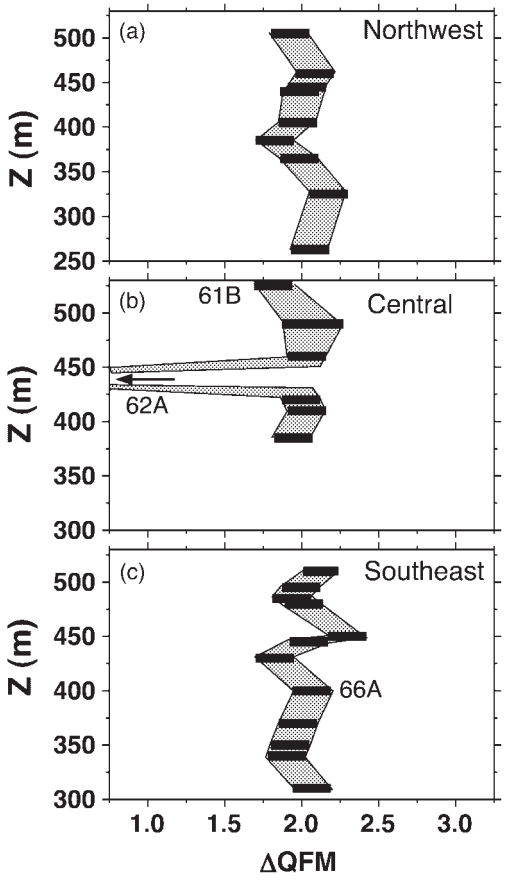

Fig. 10. Regional profiles of ΔQFM across layering for the northwestern, central, and southeastern parts of the field area (Fig. 1). Z is the elevation of the sample in meters above sea level. Length of black bars corresponds to ΔQFM calculated for the range in magnetite activities from 0·75 to 1·0 (see text, Table 7). Sample 62A plots off-scale at ΔQFM −0·75. Samples 61B and 66A discussed in text.

the $\log_{10}(a_{Mg^{2+}}/a_{Fe^{2+}})$ would vary more strongly as a function of fluid Fe^{3+}/Fe^{2+}.

In contrast, $\log_{10}(a_{Mn^{2+}}/a_{Fe^{2+}})$ varies significantly and shows a weak positive correlation with f_{O_2} (Fig. 11). In most cases the $\log_{10}(a_{Mn^{2+}}/a_{Fe^{2+}})$ variations are not abrupt and restricted to individual beds, but rather are gradational at the 10–100 m scale. Examples include the gradual decrease in $\log_{10}(a_{Mn^{2+}}/a_{Fe^{2+}})$ from 460 to 360 m in the northwest profile (Fig. 11a), and the 'C'-shaped variation between 300 and 425 m in the southeast profile (Fig. 11c). The sharper discontinuity in the central profile corresponds to the extremely low f_{O_2} sample 62A, and may be of metasomatic origin (see below). Metamorphic fluid–rock interaction was insufficient to homogenize fluid Mn^{2+}/Fe^{2+} in the sequence, possibly owing to low Mn concentrations in fluids (i.e. large solid–fluid partition coefficient for Mn).

DISCUSSION OF f_{O_2} SYSTEMATICS

Chinner (1960) used the rock oxidation ratio (OR) as an index of rock oxidation state, where $OR = 2Fe_2O_3 \times 100/(2Fe_2O_3 + FeO)$ (molecular basis). Although clearly powerful, OR is not a direct indicator of f_{O_2} because rocks of differing OR can equilibrate at the same f_{O_2}. For example, for equilibrium at a given P and T, pore fluid in a rock that contains 99% Hem and 1% Mag would be at the same f_{O_2} as fluid in a rock containing 99% Mag and 1% Hem, even though the OR values for the two rocks differ considerably.

In fact, a wide range of OR values, between about 20 and 50, are compatible with essentially the same ΔQFM of about +2 (Fig. 12). Consequently, the observation of intimately interbedded rocks of differing OR (Chinner, 1960) does not necessarily indicate that the rocks had very different f_{O_2} and fluid compositions. Extremes of the OR range are, however, associated with extremes of f_{O_2}. Sample 62A, equilibrated at ΔQFM <0, has OR <20, whereas sample 11 of Chinner (1960) has an OR of ∼75 and ΔQFM > +2·5. These extremes of the f_{O_2} range are discussed in a later section.

The homogeneity of the bulk of the metamorphic f_{O_2} values can be interpreted in two ways. One possibility is that the lack of large variations reflects a protolith that was fairly homogeneous with respect to mineral and fluid compositions to start with (although OR values must

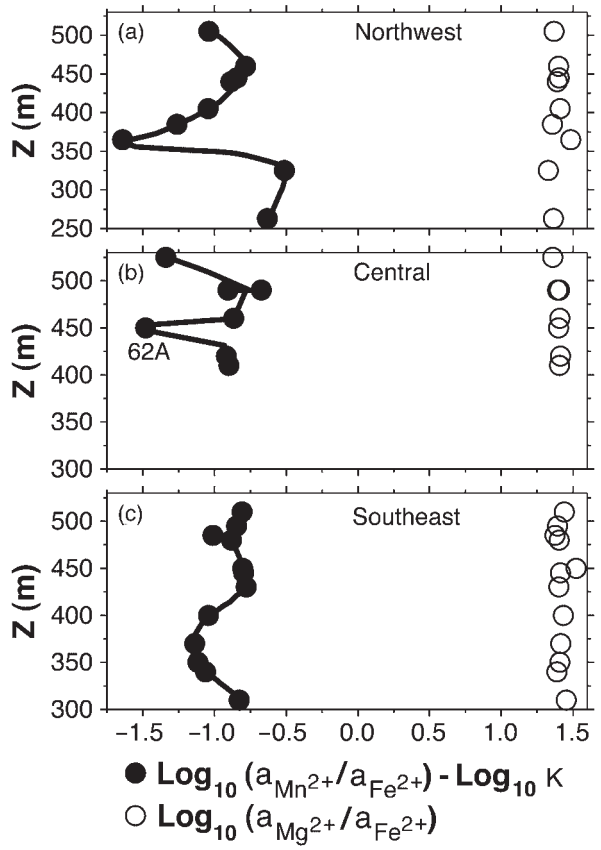

Fig. 11. Elevation (Z) in meters above sea level vs fluid $\log_{10}(a_{Mn^{2+}}/a_{Fe^{2+}}) - \log_{10} K$ [reaction (10)] and $\log_{10}(a_{Mg^{2+}}/a_{Fe^{2+}})$ [reaction (9)] for northwestern, central, and southeastern profiles.

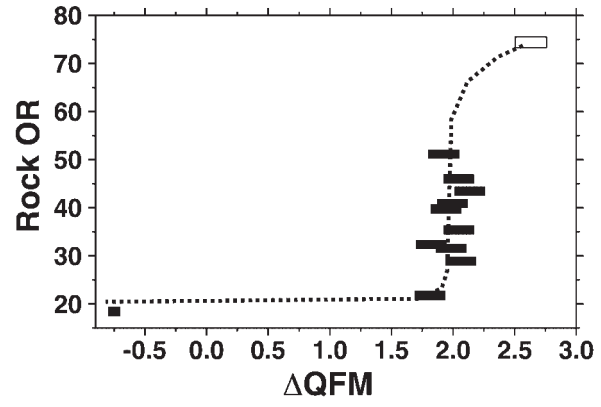

Fig. 12. Rock oxidation ratio (OR) vs ΔQFM. High f_{O_2} sample 11 of Chinner (1960) denoted by open rectangle.

have differed from bed to bed). Metamorphism of such a sequence would not be expected to produce large gradients in f_{O_2} and fluid composition between layers, unless 'exotic', nonequilibrium fluids from outside the sequence were introduced.

The second possibility is that the sequence was originally more heterogeneous, such that sharp, layer-to-layer variations in redox state controlled by protolith composition existed. Metamorphic fluid–rock interaction between layers must then have acted to smooth these short wavelength variations so that the entire sequence attained a relatively uniform redox state. The observed increases in the X_{Ilm} and decreases in the X_{Hem} of RHOMOX inclusions from core to rim in garnet (Figs 2 and 8) suggest that some syn-metamorphic changes in redox state did occur.

If redox states were homogenized during metamorphism, the reaction histories would have been critically dependent on fluid compositions and the amount of fluid transport. The highly oxidized, ΔQFM +2 fluids of Mag-bearing rocks would have been fairly inefficient oxidizers or reducers because such fluids consist mostly of H_2O and CO_2, and are poor in many species needed for redox reactions including H_2, CH_4, and CO (Wood & Walther, 1986; Frost, 1991*a*; Ague, 1998). For example, the reactions

$$3H_2 + 3Hem + Ms + 3Qtz = Ann + Alm + 3H_2O \quad (11)$$

$$0{\cdot}75CH_4 + 3Hem + Ms + 3Qtz = Ann + Alm + 0{\cdot}75CO_2 + 1{\cdot}5H_2O \quad (12)$$

require either 1 mole of H_2 or 0·25 moles of CH_4 to reduce 1 mole of Hem and produce garnet and biotite. Typical ΔQFM +2 Glen Clova fluids, however, probably had X_{H_2} of only $\sim 10^{-4}$ and vanishingly small $X_{CH_4} < \sim 10^{-7}$ (Table 8). Consequently, large fluid–rock ratios would have been needed to homogenize the rock package. Quantification of these ratios is difficult owing to the uncertain activity–composition relations for RHOMOX, but calculations using simple model reactions such as (11) and (12), and representative fluid compositions (Table 8) and modes (Chinner, 1960) imply that if homogenization occurred, minimum fluid–rock ratios were $\sim 10^2$ (Wood & Walther, 1986; Ague, 1998). Fluid exchange between beds would probably have been dominated by diffusion and mechanical dispersion across layers (e.g. Ague & Rye, 1999; Baxter & DePaolo, 2000), although advection may also have played a role. Modeling results suggest that disruption of protolith bed-scale fugacity heterogeneities may occur in as little as $10^2 - 10^3$ years (Ague, 1998).

PETROGENESIS OF SAMPLES AT THE EXTREMES OF THE f_{O_2} RANGE

Rocks equilibrated at extremely low f_{O_2}

Two samples (46B, 62A), making up ~6% of the sample set, are from layers that equilibrated at f_{O_2} 2–3 orders of magnitude lower than the rest of the rocks. The layers

Table 8: Fluid mole fractions

Species	Representative ΔQFM +1·8 X_{H_2O} = 0·50*	Representative ΔQFM +1·8 X_{H_2O} = 0·95*	Representative ΔQFM +2·4 X_{H_2O} = 0·50*	Representative ΔQFM +2·4 X_{H_2O} = 0·95*	Sample 62A ΔQFM −0·75
H_2	$1·18 \times 10^{-4}$	$1·78 \times 10^{-4}$	$5·93 \times 10^{-5}$	$8·91 \times 10^{-5}$	$3·01 \times 10^{-2}$
H_2O	$5·00 \times 10^{-1}$	$9·50 \times 10^{-1}$	$5·00 \times 10^{-1}$	$9·50 \times 10^{-1}$	$8·04 \times 10^{-1}$
CO_2	$4·96 \times 10^{-1}$	$4·44 \times 10^{-2}$	$4·98 \times 10^{-1}$	$4·71 \times 10^{-2}$	$1·71 \times 10^{-1}$
CO	$2·13 \times 10^{-4}$	$4·35 \times 10^{-5}$	$1·07 \times 10^{-4}$	$2·29 \times 10^{-5}$	$2·10 \times 10^{-3}$
CH_4	$1·28 \times 10^{-7}$	$5·90 \times 10^{-8}$	$8·09 \times 10^{-9}$	$3·91 \times 10^{-9}$	$1·53 \times 10^{-2}$
H_2S	$3·39 \times 10^{-3}$	$5·10 \times 10^{-3}$	$1·70 \times 10^{-3}$	$2·55 \times 10^{-3}$	$2·68 \times 10^{-3}$
SO_2	$6·00 \times 10^{-5}$	$6·00 \times 10^{-5}$	$2·39 \times 10^{-4}$	$2·39 \times 10^{-4}$	$7·55 \times 10^{-9}$
COS	$3·02 \times 10^{-4}$	$6·17 \times 10^{-5}$	$1·52 \times 10^{-4}$	$3·25 \times 10^{-5}$	$1·33 \times 10^{-4}$
S_2	$1·56 \times 10^{-6}$	$1·56 \times 10^{-6}$	$1·56 \times 10^{-6}$	$1·56 \times 10^{-6}$	$3·11 \times 10^{-9}$
$a_{Graphite}$	$5·39 \times 10^{-3}$	$1·10 \times 10^{-3}$	$1·36 \times 10^{-3}$	$2·90 \times 10^{-4}$	$1·00 \times 10^{0}$
ΔPyPo†	−0·25	−0·25	−0·25	−0·25	−2·95

*Calculated for representative range in X_{H_2O} based on McLellan (1985).
†ΔPyPo is the difference between $\log_{10} f_{S_2}$ for the fluid and $\log_{10} f_{S_2}$ for the pyrite–pyrrhotite buffer at 660°C and 5·7 kbar.

are at least meter scale in thickness, but whether contacts with surrounding rocks are sharp, gradational, tectonic, or otherwise could not be determined in the field. Either the sedimentary or diagenetic precursors to these two samples were highly reduced, or reduction resulted from metamorphic fluid–rock interaction. Some evidence from graphite and fluorine systematics suggests the latter possibility.

Graphite, inferred to have been derived from sedimentary organic matter, is common in low-OR rocks far removed (kilometer scale) from the study area (Chinner, 1960). In contrast, graphite is absent from the lowest f_{O_2} sample (62A). This sample probably originally lacked or contained only traces of organic matter and, thus, its protolith may not have been highly 'reduced'. Consequently, the low f_{O_2} could have been produced during metamorphism.

Traces of graphite may be included within a few mica grains in 46B, but the identification is uncertain. On the other hand, the sample is cut by millimeter- to centimeter-wide, post-peak metamorphic shear zones containing abundant carbonaceous material, plagioclase, muscovite, and chlorite, and minor calcite (Fig. 13). Reducing fluids were therefore able to infiltrate the rock, albeit not necessarily on the prograde path.

The low f_{O_2} samples record larger HF/H_2O than the others (Fig. 14). In addition, sample 46B is cut by veins that contain abundant F-rich tourmaline crystals as much as 1 cm long of probable metasomatic origin (see Dutrow *et al.*, 1999). We suggest that the HF/H_2O systematics reflect the local infiltration of chemically active fluids into the low f_{O_2} rocks, and draw the connection that these fluids also drove syn-metamorphic reduction. The HF/H_2O relations might also have been inherited from sedimentary protoliths, but it is difficult to envision what sedimentary process could produce a negative correlation between HF/H_2O and ΔQFM (Fig. 14).

The above evidence suggests that infiltration of reduced metamorphic fluids drove reaction and lowered f_{O_2} in samples 46B and 62A. If these fluids were at or near graphite saturation, they would have contained abundant H_2 and CH_4 (sample 62A, Table 8). Because these species are powerful reducing agents, alteration would have occurred even if fluid–rock ratios were rather small—of the order of one or less (Wood & Walther, 1986; Ague, 1998). The fluid could have been derived from graphitic rocks, such as those that surround the sequence studied here, or from reduced magmas that intruded during peak metamorphism. If the low f_{O_2} was produced during metamorphism, the localized reduction suggests channelized fluid infiltration.

High f_{O_2} sample

Sample 11 of Chinner (1960) has both large OR and ΔQFM relative to our samples (Fig. 12). These characteristics were probably inherited from the protolith because (1) the large Mn and Fe contents of the rock suggest a protolith with high bulk-rock Fe_2O_3/FeO [see discussion by Chinner (1960)], and (2) no local or regional sources for highly oxidized metamorphic fluids needed

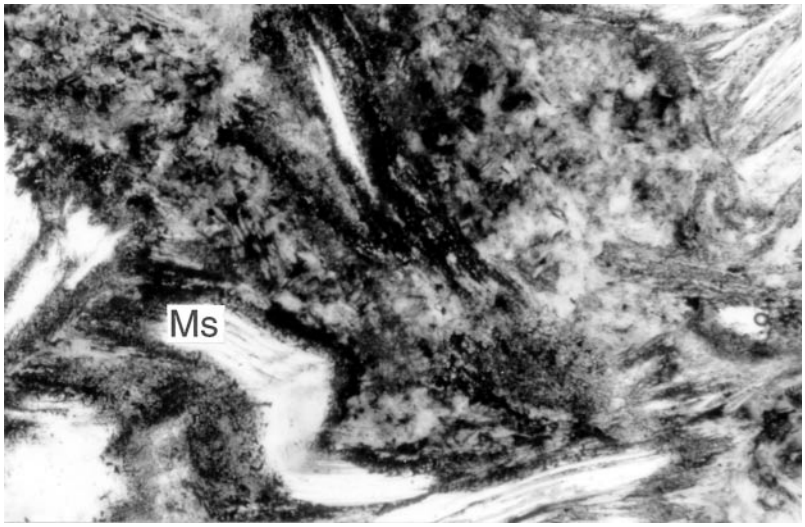

Fig. 13. Photomicrograph of post-peak metamorphic shear zone in sample 46B. Deformed muscovite grains (Ms) lie within chlorite-rich matrix. Note abundant dust-like carbonaceous material. Field of view 1·35 mm wide; plane-polarized light.

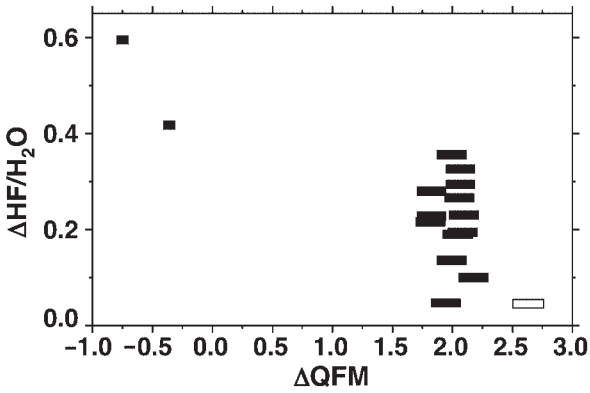

Fig. 14. $\Delta HF/H_2O$ vs ΔQFM. $\Delta HF/H_2O$ is the difference in $\log_{10}(f_{HF}/f_{H_2O})$ between the sample and $\log_{10}(f_{HF}/f_{H_2O})$ for a standard biotite having $X_{Mg} = 0{\cdot}5$ and $\log_{10}(X_F/X_{OH}) = -1{\cdot}5$ at 660°C and 5·7 kbar. High f_{O_2} sample 11 of Chinner (1960) denoted by open rectangle. F in this sample was below detection (Chinner, 1960). Its F content was set to the smallest value measured from our sample suite and thus probably represents a maximum.

to oxidize the rock are evident. One possibility is that sample 11 is an unusual relic that escaped to some degree redox equilibration with the rest of the sequence, perhaps because of extremely low porosity and/or permeability. Another possibility is that the bulk garnet composition of Chinner (1960) used in our calculations has lower Fe/Mn and almandine activity than the peak-T rim composition. If so, then the f_{O_2} estimate made using the bulk garnet composition would be somewhat too high.

CONCLUSION

Estimated f_{O_2} for the bulk of the study area was about $+2\ \log_{10}$ units above the quartz–fayalite–magnetite buffer (ΔQFM $\sim +2$) at sillimanite zone conditions, although rare low f_{O_2} rocks (ΔQFM <0) were also present. The high f_{O_2} of ΔQFM $\sim +2$ is comparable with the highest known from arc settings (e.g. dacite from Mt Pinatubo; Evans & Scaillet, 1997). With the exception of the rare low f_{O_2} rocks, variations in metamorphic f_{O_2} across the study area were generally small, about $\pm 0{\cdot}3\ \log_{10}$ units. This minimal variability may reflect either (1) a protolith that was initially homogeneous with respect to redox state or (2) a protolith characterized by significant differences in redox state from bed to bed that was homogenized by metamorphic fluid–rock interaction. Rhombohedral oxide (RHOMOX) inclusions in garnet grains that become richer in ilmenite and poorer in hematite towards garnet rims suggest that some syn-metamorphic reduction of rock occurred. In detail, the ΔQFM $\sim +2$ rocks comprise intimately intercalated, graphite-free metasedimentary layers with whole-rock oxidation ratios (OR) that vary mostly between ~ 20 and ~ 50 from one layer to the next [OR = molecular $2Fe_2O_3 \times 100/(2Fe_2O_3 + FeO)$]. These OR variations are probably inherited from sedimentary protoliths, are uncorrelated with f_{O_2}, and do not indicate that large, order-of-magnitude gradients in f_{O_2} and redox state existed between these layers during metamorphism. As pointed out by Chinner (1960), metamorphic fluid–rock interaction did not homogenize fluid compositions at scales of several kilometers, because the high f_{O_2}, ΔQFM $\sim +2$ rocks are in regional contact with Fe_2O_3-poor, graphite-bearing lithologies. The rare low f_{O_2} rocks (ΔQFM <0) in our field area that occur among the dominant high f_{O_2} (ΔQFM $\sim +2$) rocks may have been reduced by regionally migrating fluids derived from these graphite-bearing surroundings.

ACKNOWLEDGEMENTS

We thank D. M. Rye, E. L. McLellan, R. L. Masters, and C. J. Carson for thoughtful discussions, M. S. Ghiorso for sharing both software and insightful advice for calculating activity–composition relations among Fe–Ti oxides, B. W. Evans, B. R. Frost, and an anonymous referee for critical reviews, and S. S. Sorensen for editorial handling. Financial support from the National Science Foundation, Division of Earth Sciences, grant EAR-9405889, is gratefully acknowledged.

REFERENCES

Ague, J. J. (1998). Simple models of coupled fluid infiltration and redox reactions in the crust. *Contributions to Mineralogy and Petrology* **132**, 180–197.

Ague, J. J. & Brimhall, G. H. (1988). Magmatic arc asymmetry and distribution of anomalous plutonic belts in the batholiths of California: effects of assimilation, cratonal thickness, and depth of crystallization. *Geological Society of America Bulletin* **100**, 912–927.

Ague, J. J. & Rye, D. M. (1999). Simple models of CO_2 release from metacarbonates with implications for interpretation of directions and magnitudes of fluid flow in the deep crust. *Journal of Petrology* **40**, 1443–1462.

Andersen, D. J. & Lindsley, D. H. (1988). Internally consistent solution models for the Fe–Mg–Mn–Ti oxides: Fe–Ti oxides. *American Mineralogist* **73**, 714–726.

Baxter, E. F. & DePaolo, D. J. (2000). Field measurement of slow metamorphic reaction rates at temperatures of 500° to 600°C. *Science* **288**, 1411–1414.

Baxter, E. F., Ague, J. J. & DePaolo, D. J. (2000). Tectonometamorphic history of the Barrovian type-locality constrained by precise Sm/Nd garnet ages from Glen Clova, Scotland. *Geological Society of America, Abstracts with Programs,* **32**, A-153.

Berman, R. G. (1988). Internally-consistent thermodynamic data for minerals in the system Na_2O–K_2O–CaO–MgO–FeO–Fe_2O_3–Al_2O_3–SiO_2–TiO_2–H_2O–CO_2. *Journal of Petrology* **29**, 445–522.

Berman, R. G. (1990). Mixing properties of Ca–Mg–Fe–Mn garnets. *American Mineralogist* **75**, 328–344.

Berman, R. G. (1991). Thermobarometry using multi-equilibrium calculations: a new technique, with petrological applications. *Canadian Mineralogist* **29**, 833–855.

Berman, R. G. & Aranovich, L. Ya. (1996). Optimized standard state and solution properties of minerals I. Model calibration for olivine, orthopyroxene, cordierite, garnet, and ilmenite in the system FeO–MgO–CaO–Al_2O_3–TiO_2–SiO_2. *Contributions to Mineralogy and Petrology* **126**, 1–24.

Brenan, J. M., Shaw, H. F., Ryerson, F. J. & Phinney, D. L. (1995). Mineral–aqueous fluid partitioning of trace elements at 900°C and 2·0 GPa: constraints on the trace element chemistry of mantle and deep crustal fluids. *Geochimica et Cosmochimica Acta* **59**, 3331–3350.

Buddington, A. F. & Lindsley, D. H. (1964). Iron–titanium oxide minerals and synthetic equivalents. *Journal of Petrology* **5**, 310–357.

Burton, B. P. (1991). The interplay of chemical and magnetic ordering. In: Lindsley, D. H. (ed.) *Oxide Minerals. Mineralogical Society of America, Reviews in Mineralogy* **25**, 303–321.

Chatterjee, N. D. & Froese, E. (1975). A thermodynamic study of the pseudobinary join muscovite–paragonite in the system $KAlSi_3O_8$–$NaAlSi_3O_8$–Al_2O_3–SiO_2–H_2O. *American Mineralogist* **60**, 985–993.

Chinner, G. A. (1960). Pelitic gneisses with varying ferrous/ferric ratios from Glen Clova, Angus, Scotland. *Journal of Petrology* **1**, 178–217.

Chinner, G. A. (1961). The origin of sillimanite in Glen Clova, Angus. *Journal of Petrology* **2**, 312–323.

Deer, W. A., Howie, R. A. & Zussman, J. (1992). *An Introduction to the Rock-Forming Minerals*. Harlow: Longman.

Dempster, T. J. & Bluck, B. J. (1995). Regional metamorphism in transform zones during supercontinent breakup: Late Proterozoic events of the Scottish Highlands. *Geology* **23**, 991–994.

Dutrow, B. L., Foster, C. T., Jr & Henry, D. J. (1999). Tourmaline-rich pseudomorphs in sillimanite zone metapelites: demarcation of an infiltration front. *American Mineralogist* **84**, 794–805.

Eugster, H. P. & Skippen, G. B. (1967). Igneous and metamorphic reactions involving gas equilibria. In: Ableson, P. H. (ed.) *Researches in Geochemistry II*. New York: John Wiley, pp. 492–520.

Evans, B. W. & Scaillet, B. (1997). The redox state of Pinatubo dacite and the ilmenite hematite solvus. *American Mineralogist* **82**, 625–629.

Ferry, J. M. & Baumgartner, L. P. (1987). Thermodynamic models of molecular fluids at the elevated pressures and temperatures of crustal metamorphism. In: Carmichael, I. S. E. & Eugster, H. P. (eds) *Thermodynamic Modeling of Geological Materials: Minerals, Fluids, and Melts. Mineralogical Society of America, Reviews in Mineralogy* **17**, 323–365.

Fettes, D. J., Graham, C. M., Harte, B. & Plant, J. A. (1986). Lineaments and basement domains: an alternative view of Dalradian evolution. *Journal of the Geological Society, London* **143**, 453–464.

French, B. M. (1966). Some geological implications of equilibrium between graphite and a C–O–H gas phase at high temperatures and pressures. *Reviews of Geophysics* **4**, 223–253.

Frost, B. R. (1991*a*). Introduction to oxygen fugacity and its petrologic importance. In: Lindsley, D. H. (ed.) *Oxide Minerals. Mineralogical Society of America, Reviews in Mineralogy* **25**, 1–9.

Frost, B. R. (1991*b*). Stability of oxide minerals in metamorphic rocks. In: Lindsley, D. H. (ed.) *Oxide Minerals. Mineralogical Society of America, Reviews in Mineralogy* **25**, 469–487.

Ghiorso, M. S. (1990). Thermodynamic properties of hematite–ilmenite–geikielite solid solutions. *Contributions to Mineralogy and Petrology* **104**, 645–667.

Ghiorso, M. S. & Sack, R. O. (1991). Fe–Ti oxide geothermometry: thermodynamic formulation and the estimation of intensive variables in silicic magmas. *Contributions to Mineralogy and Petrology* **108**, 485–510.

Harlov, D. E., Newton, R. C., Hansen, E. C. & Janardhan, A. S. (1997). Oxide and sulfide minerals in highly oxidized, Rb-depleted, Archaean granulites of the Shevaroy Hills massif, South India: oxidation states and the role of metamorphic fluids. *Journal of Metamorphic Geology* **15**, 701–717.

Harry, W. T. (1958). A re-examination of Barrow's older granites in Glen Clova, Angus. *Transactions of the Royal Society of Edinburgh* **63**, 393–413.

Harte, B. (1975). Displacement of the kyanite isograd by local variations in oxygen fugacity within pelitic schists in Glen Lethnot, Angus, Scotland. *Transactions of the American Geophysical Union* **56**, 466.

Harte, B. & Johnson, M. R. W. (1969). Metamorphic history of Dalradian rocks in Glens Clova, Esk, and Lethnot, Angus, Scotland. *Scottish Journal of Geology* **5**, 56–80.

Harte, B., Booth, J. E., Dempster, T. J., Fettes, D. J., Mendum, J. R. & Watts, D. (1984). Aspects of the post-depositional evolution of Dalradian and Highland Boundary rocks in the southern Highlands of Scotland. *Transactions of the Royal Society of Edinburgh, Earth Sciences* **75**, 151–163.

Holloway, J. R. (1987). Igneous fluids. In: Carmichael, I. S. E. & Eugster, H. P. (eds) *Thermodynamic Modeling of Geological Materials: Minerals, Fluids, and Melts. Mineralogical Society of America, Reviews in Mineralogy* **17**, 211–233.

James, H. L. (1955). Zones of regional metamorphism in the Pre-Cambrian of northern Michigan. *Geological Society of America Bulletin* **66**, 1455–1488.

Johnson, J. W., Oelkers, E. H. & Helgeson, H. C. (1992). SUPCRT92: a software package for calculating the standard molal thermodynamic properties of minerals, gases, aqueous species, and reactions from 1 to 5000 bars and 0° to 1000°C. *Computers and Geosciences* **18**, 899–947.

Kerrick, D. M. & Jacobs, G. K. (1981). A modified Redlich–Kwong equation for H_2O, CO_2, and H_2O–CO_2 mixtures at elevated temperatures and pressures. *American Journal of Science* **281**, 735–767.

Kretz, R. (1983). Symbols for rock-forming minerals. *American Mineralogist* **68**, 277–279.

Lamb, W. M. & Valley, J. W. (1985). C–O–H fluid calculations and granulite genesis. In: Tobi, A. & Touret, J. (eds) *The Deep Proterozoic Crust in the North American Provinces*. Dordrecht: D. Reidel, pp. 119–131.

McLellan, E. L. (1985). Metamorphic reactions in the kyanite and sillimanite zones of the Barrovian type area. *Journal of Petrology* **26**, 789–818.

McLellan, E. L. (1989). Sequential formation of subsolidus and anatectic migmatites in response to thermal evolution, eastern Scotland. *Journal of Geology* **97**, 165–182.

McMullin, D. W. A., Berman, R. G. & Greenwood, H. J. (1991). Calibration of the SGAM thermobarometer for pelitic rocks using data from phase-equilibrium experiments and natural assemblages. *Canadian Mineralogist* **29**, 889–908.

Miyashiro, A. (1964). Oxidation and reduction in the Earth's crust with special reference to the role of graphite. *Geochimica et Cosmochimica Acta* **28**, 717–729.

Ohmoto, H. & Kerrick, D. M. (1977). Devolatilization equilibria in graphitic systems. *American Journal of Science* **277**, 1013–1044.

Oliver, G. J. H., Chen, F., Buchwaldt, R. & Hegner, E. (2000). Fast tectonometamorphism and exhumation in the type area of the Barrovian and Buchan zones. *Geology* **28**, 459–462.

Robie, R. A., Hemingway, B. S. & Fisher, J. R. (1979). Thermodynamic properties of minerals and related substances at 298·15 K and 1 bar (10^5 Pascals) pressure and at higher temperatures. *US Geological Survey Bulletin* **1452**, 456 pp.

Rogers, G., Dempster, T. J., Bluck, B. J. & Tanner, P. W. G. (1989). A high-precision U–Pb age for the Ben Vuirich granite: implications for the evolution of the Scottish Dalradian Supergroup. *Journal of the Geological Society, London* **146**, 789–798.

Rumble, D., III (1978). Mineralogy, petrology, and oxygen isotopic geochemistry of the Clough Formation, Black Mountain, western New Hampshire, U.S.A. *Journal of Petrology* **19**, 317–340.

Shi, P. & Saxena, S. K. (1992). Thermodynamic modeling of the C–H–O–S fluid system. *American Mineralogist* **77**, 1038–1049.

Shock, E. L., Sassani, D. C., Willis, M. & Sverjensky, D. A. (1997). Inorganic species in geologic fluids: correlations among standard molal thermodynamic properties of aqueous ions and hydroxide complexes. *Geochimica et Cosmochimica Acta* **61**, 907–950.

Stull, D. R. & Prophet, H. (1971). JANAF thermochemical tables. *Standard Reference Data Series, US National Bureau of Standards* **37**, 1141 pp.

Sverjensky, D. A., Shock, E. L. & Helgeson, H. C. (1997). Prediction of the thermodynamic properties of aqueous metal complexes to 1000°C and 5 kb. *Geochimica et Cosmochimica Acta* **61**, 1359–1412.

Thompson, J. B., Jr (1970). Geochemical reaction and open systems. *Geochimica et Cosmochimica Acta* **34**, 529–551.

Wagman, D. D., Evans, W. H., Parker, V. B., Schumm, R. H., Harlow, I., Bailey, S. M., Churney, K. L. & Nuttall, R. L. (1982). The NBS tables of chemical thermodynamic properties. *Journal of Physical and Chemical Reference Data, Supplement Number 2* **11**, 392 pp.

Wones, D. R. & Eugster, H. P. (1965). Stability of biotite: experiment, theory, and application. *American Mineralogist* **50**, 1228–1272.

Wood, B. J. & Walther, J. V. (1986). Fluid flow during metamorphism and its implications for fluid–rock ratios. In: Walther, J. V. & Wood, B. J. (eds) *Fluid–Rock Interactions during Metamorphism*. New York: Springer, pp. 89–107.

Zhu, C. & Sverjensky, D. A. (1992). F–Cl–OH partitioning between biotite and apatite. *Geochimica et Cosmochimica Acta* **56**, 3435–3467.

APPENDIX: ANALYTICAL AND DATA REDUCTION PROCEDURES

Mineral composition determinations and electron microscopy used the JEOL JXA-8600 electron microprobe at Yale University. Quantitative analyses employed wavelength-dispersive spectrometers, 20 nA Faraday cup current, 15 kV accelerating voltage, natural and synthetic standards, off-peak and fluorescence-corrected, non-linear mean atomic number background corrections, and $\varphi(\sigma z)$ matrix corrections. Electron microscope image processing and qualitative energy-dispersive chemical analyses were carried out with systems mounted on the JXA-8600; the early stages of our study used a Kevex Delta system and the later stages used an EDAX Phoenix system.

All Fe was assigned to FeO for the matrix corrections. This procedure can lead to inaccurate results for Fe^{3+}-rich phases if the 'excess' oxygen associated with Fe_2O_3 is not accounted for. Consequently, oxygen was incorporated by difference into the matrix correction iterations for RHOMOX and Mag such that the sum of all oxides and the 'excess' oxygen was 100 wt %. Similarly, H_2O was specified by difference in the matrix corrections for micas such that the sum of the oxides and the H_2O was 100 wt %.

Bulk compositions for the exsolved RHOMOX were estimated by making as many as 40 spot determinations on several grains per thin section. A 5 or 10 μm diameter beam was used in nearly all cases, but a focused beam was required for several fine-grained samples. Data were typically collected along linear traverses perpendicular to the long axes of the exsolution lamellae. At least five spot analyses on 1–2 grains per thin section were carried out for unexsolved RHOMOX (10 μm beam), Rt (5 μm beam), Mag (focused beam), garnet (focused beam), and micas (15 or 20 μm beam). Linear traverses across garnet involved as many as 50 determinations. Unless noted otherwise, reported garnet analyses are for inferred 'peak' compositions having the highest Mg and lowest Mn contents (usually several tens of μm from the rim).

Structural formulae for RHOMOX and magnetite were computed assuming 2 moles of cations per three oxygens for RHOMOX, and 3 moles of cations per four oxygens for magnetite. These procedures were judged successful because total oxide sums incorporating estimated FeO and Fe_2O_3 are always near 100 wt % (Tables 3 and 4). FeO and Fe_2O_3 in garnet can be estimated in several ways; we assumed 2 moles of octahedrally coordinated cations per 12 oxygens. This procedure gives the best results when tested against the wet chemical determinations by Deer *et al.* (1992), and gives total cation site occupancies very close to the ideal number of three for the four-fold and eight-fold coordinated sites (Table 6).

Bulk-rock X-ray fluorescence analyses were performed by X-ray Assay Laboratories, Don Mills, Ontario, Canada. FeO was determined using standard wet chemical titrations.